Ocean Engineering 368 (2026) 128239



Contents lists available at ScienceDirect

Ocean Engineering

journal homepage: www.elsevier.com/locate/oceaneng



Research paper

Motion responses and flow field characteristics of a CFPSO with complex heave plates under regular waves

Yisheng Yao [a], Jingwen Zhang [b], Gang Li [b], Weiwen Zhao [a,*], Decheng Wan [a]

[a] Computational Marine Hydrodynamics Lab (CMHL), School of Naval Architecture, Ocean and Civil Engineering, Shanghai Jiao Tong University, Shanghai, 200240, China
[b] CNOOC Research Institute, Beijing, China

ARTICLE INFO

Keywords:
CFPSO
Complex heave plate
CFD method
Naoe-FOAM-SJTU
Flow field characteristics

ABSTRACT

Cylindrical floating production storage and offloading (CFPSO) units are widely recognized as superior platforms in the field of offshore oil and gas engineering. Practical engineering applications show that heave plates not only have significant effects on heave motion, but also exert coupled effects on surge, pitch and slow-drift responses. However, existing academic studies are mostly limited to simple structural configurations, and systematic research on complex heave plates and their influences on multi-degree-of-freedom motions is still insufficient. In this paper, based on the computational fluid dynamics (CFD) method and using the in-house code naoe-FOAM-SJTU, the effects of complex heave plates with serrated protrusions, edge-cutting and openings on the motion performance of a CFPSO are investigated under different wave-facing configurations. The numerical model is calibrated and validated against model test data. Typical operating conditions are determined through free-decay tests, and three characteristic motion patterns are summarized by analyzing the motion responses under six wave-facing configurations. By analyzing the flow field characteristics, the motion response mechanisms are revealed. Additionally, response amplitude operator (RAO) curves for typical wave periods are calculated to verify the general applicability of the conclusions.

1. Introduction

With the development of offshore oilfield exploration and extraction technologies, the offshore oil and gas industry has achieved rapid and sustained growth over the past decade. Currently, offshore oil and gas extraction is gradually expanding from nearshore waters to deep waters, which means the extraction platforms and equipment adopted will face more severe environmental conditions. In addition, considering economic benefits such as cost, the size of extraction platforms and oil storage platforms has become increasingly large. Floating Production Storage and Offloading (FPSO) units are widely used in the offshore oil and gas industry. They are offshore oil production facilities that integrate production, extraction, storage, and offloading functions in one platform. The traditional FPSO form is mainly ship-shaped, and a single-point mooring system is adopted to fix it in a specific working water area (Wei et al., 2011), (Wei et al., 2012). This means that if the mooring system fails, it will cause irreparable losses (Fontaine et al., 2013). In addition, due to the inherent shape characteristics of the ship, the ship-shaped FPSO is extremely sensitive to wave direction. The huge wave loads and frequent yaw movements will further increase the risk of mooring failure. In addition, ship-shaped FPSOs typically demonstrate inferior roll and heave performance.

Consequently, numerous scholars have put forward corresponding innovative schemes. The Sevan Piranema, designed by the Sevan team, is the world's first cylindrical FPSO unit to be put into commercial operation (Saad et al., 2009). Cylindrical FPSO are characterized by a simple design and low cost, and have been widely applied in offshore engineering. However, as the main body of a cylindrical FPSO is a cylinder, this type of floating structure typically exhibits significant motion responses under wave action (Gonçalves et al., 2009a; Gonçalves et al., 2009b). In particular, when confronted with complex operating environments, they are associated with considerable safety risks (Wang et al., 2017a). Based on the designs of previous researchers, many scholars have carried out improvements and innovations in the structural design of cylindrical FPSO, aiming to achieve better stability and safety. Wang et al. (2017b), (Wang et al., 2016) modified the traditional cylindrical FPSO by narrowing its midsection and increasing the diameter of its bottom, developing a novel hourglass-shaped FPSO. On the

* Corresponding author.
E-mail address: weiwen.zhao@sjtu.edu.cn (W. Zhao).

https://doi.org/10.1016/j.oceaneng.2026.128239
Received 25 March 2026; Received in revised form 22 July 2026; Accepted 15 September 2026
Available online 25 September 2026
0029-8018/© 2026 Published by Elsevier Ltd.

premise of not sacrificing internal space, this design improves the platform stability. The results indicate that the new hourglass-shaped FPSO can not only shift the peak pitch frequency away from the high-energy spectrum range of waves but also enhance the platform restoring moment, ultimately reducing the platform pitch response by approximately 33%. In addition to pitch performance, heave performance is also a crucial factor influencing the motion of cylindrical FPSO platforms. Regarding heave motion suppression, substantial experience has been accumulated in numerous platform designs—specifically, installing heave plates at the bottom of platform to generate vortex shedding flows, thereby providing additional heave damping. (Li et al., 2013a), (Sathia and Vijayalakshmi, 2019). Tao et al. (Tao and Cai, 2004) investigated the influence of the proportional relationship between different cylinder diameters and heave plate diameters on the heave motion of cylindrical FPSOs via numerical methods, as shown in Fig. 1. Ultimately, they concluded that the heave plate should extend at least four times the typical heave amplitude to achieve the optimal drag effect. In addition, Tao et al. (2007) adopted a finite difference method to investigate the effect of a vertical cylinder fitted with two circular-disk heave plates on heave motion. Ji et al. (2019) proposed a novel FPSO platform with a tapered angle, as shown in Fig. 2. The heave plates of this new platform do not have a uniform thickness; instead, they gradually thin from the main body outward, with small holes drilled in the edge regions. Ultimately, it was found that with reasonably designed hole diameters, the platform can effectively suppress both heave and pitch motions. Most of these studies are based on previous design experience, integrating special structures such as openings, small holes, moonpools, and serrations with heave plates to increase heave damping and suppress platform motions. However, they fail to focus on and reveal the flow details around the heave plates, nor do they explore whether there are coupling effects between these special structures. Studies on heave plates in other engineering fields have found that while heave plates can improve the heave motion of platforms, they often exert a certain influence on the surge motion. Therefore, this study will focus on the surge, heave, and pitch motions simultaneously. (Li et al., 2013b), (Yue et al., 2020), (Gu et al., 2018).

The research methods for FPSO motion characteristics can be roughly summarized into three categories: potential flow theory (Subbulakshmia et al., 2015), (Maccamy and Fuchs, 1954), (Liu and Miao, 1985), experimental measurement, and Computational Fluid Dynamics (CFD) method (Yang et al., 2025). Although numerous scholars have adopted potential flow theory to study heave plate-related problems, this method is not an optimal solution. The reason is that the mechanism by which heave plates suppress platform motions lies in generating more vortices to increase viscous damping, while the inherent defect of the inviscid assumption in potential flow theory can only be compensated for through viscous corrections (Deng et al., 2022a), (Deng et al., 2022b). The experimental measurement features relatively high accuracy and reliability, but it is costly and fails to explicitly visualize the action process of heave plates. By contrast, the CFD method can effectively address the aforementioned issues (Devolder et al., 2017). Zhang and Ishihara (2018)conducted research on the hydrodynamic coefficients of multiple heave plates using the Large Eddy Simulation (LES) method. They compared and validated their results against those obtained from physical tank tests, investigated the hydrodynamic mechanisms acting on each individual heave plate, and proposed formulas for the added mass and drag coefficients of heave plates. These formulas are applicable to single-layer and double-layer configurations and cover three different plate geometries. Guilmineau and Queutey (2002) employed the finite volume method (FVM) to solve the two-dimensional Navier-Stokes equations, investigating the influence of the width and shape of anti-roll fins on the roll damping of FPSOs. He compared and validated the results against model test data and analyzed the process by which vortices affect the pressure distribution on FPSOs. Ji et al. (2026)conducted basin experiments to investigate the seabed response around a floating column. It is found that the heave period dominates the frequency responses of free-surface fluctuations and pore pressure, while the heave amplitude governs the energy intensity of the near-field flow. Antonio et al. (Medina-Manuel et al., 2025) investigated the relationship between hole arrangements and hydrodynamic coefficients by adjusting the position and diameter of holes on heave plates while maintaining a constant perforation ratio. Meanwhile, potential flow calculations based on WAMIT were supplemented in their research. Zhang et al. (2025) conducted numerical simulations of forced oscillations of heave plates based on the overset mesh technique. The numerical model was validated against PIV experimental data, the optimal turbulence model SA-DDES was selected, and an improved numerical framework was established. Han et al. (2024) adopted the captive model test technique to investigate hydrodynamic loads under various flow parameters and heave plate geometric parameters. It is concluded that the first harmonic dominates the hydrodynamic loads, and both motion amplitude and frequency exert significant influences on hydrodynamic coefficients when the heave plate approaches the free surface.

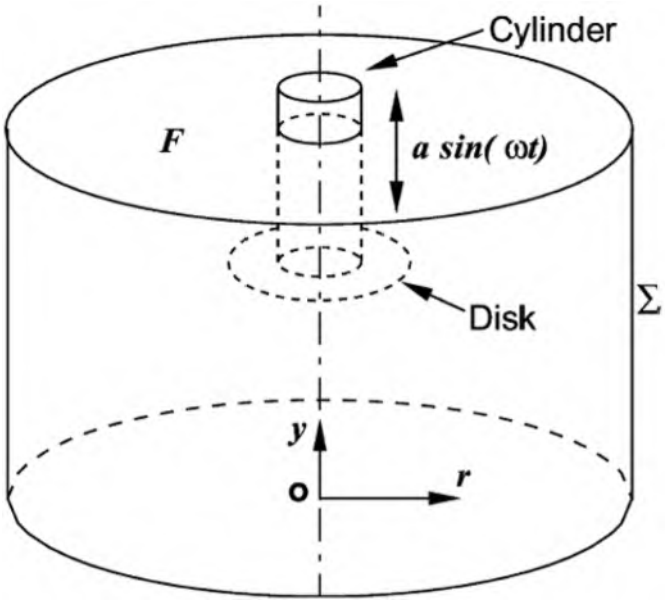

Fig. 1. A novel FPSO platform with a tapered angle (Tao and Cai, 2004), (Tao et al., 2007).

Although numerous scholars have carried out research on heave plates, most studies only adopt a single special configuration such as openings or serrations, without considering combining multiple motion-suppression configurations to exert coupling effects. Therefore, this paper designs a cylindrical FPSO (CFPSO) equipped with a composite heave plate, which integrates multiple special structures including serrations, openings and edge cuts.

In this study, numerical simulations are performed using the naoe-FOAM-SJTU solver (Zhao et al., 2020; Wang and Wan, 2018; Wang et al., 2019; Huo et al., 2023), which is developed based on the open-source software OpenFOAM. The development and validation of this solver have been elaborated in the previously published work. The research focused on the surge, heave, pitch, and low-frequency slow-drift motions of the CFPSO, while also conducting in-depth investigations into the flow details around the heave plate, the coupling effects between different structural components, and the underlying causes for the differences in motion characteristics.

The paper is organized as follows. Section 2 introduces the numerical simulation method employed in this study along with the relevant theoretical background. Section 3 describes the numerical setup, simulation conditions, and other related details, and provides thorough validation of the simulation procedure. Section 4 discusses and analyzes

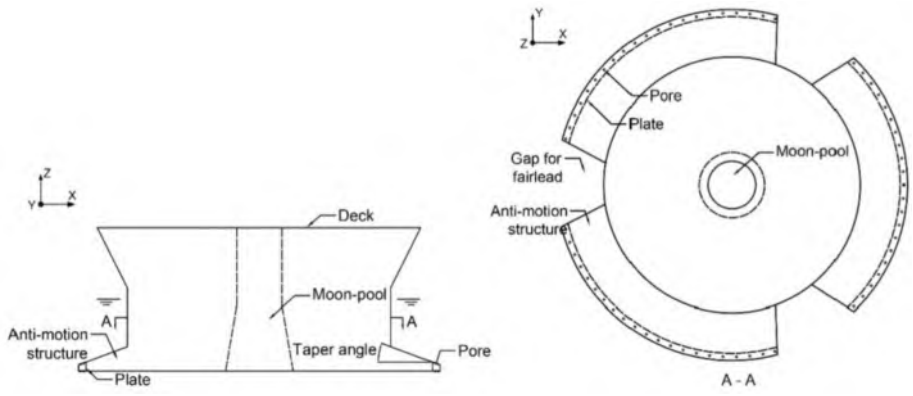

Fig. 2. A novel FPSO platform with a tapered angle (Ji et al., 2019).

the resulting motion responses, and explains the phenomena observed during the simulations using detailed flow-field data. Finally, Section 5 summarizes the main conclusions of the paper.

2. Numerical method

2.1. Governing equations

In this paper, we conduct a study on the motion response of the CFPSO under regular wave using naoe-FOAM-SJTU, an incompressible two-phase flow CFD solver developed based on OpenFOAM. The governing equations are the viscous, unsteady, and incompressible Navier-Stokes equations:

$$\nabla \cdot \boldsymbol{U} = 0 \tag{1}$$

$$\frac{\partial \rho \boldsymbol{U}}{\partial t} + \nabla \cdot \left(\rho(\boldsymbol{U} - \boldsymbol{U}_g)\boldsymbol{U}\right) = -\nabla p_d - \mathbf{g} \cdot \mathbf{x}\nabla\rho + \nabla \cdot (\mu \nabla \boldsymbol{U}) + f_\sigma \tag{2}$$

$$p_d = p - \rho \mathbf{g} \cdot \mathbf{x} \tag{3}$$

where $\boldsymbol{U}$ is the flow field velocity, $\boldsymbol{U}_g$ is the deformation velocity of the dynamic mesh, p_d is the flow field dynamic pressure, p is the total pressure of the flow field, g is the gravitational acceleration, x is the position vector of the fluid element, ρ is the fluid density, f_σ is the surface tension term, μ is the dynamic viscosity coefficient of the fluid, t is time.

This study investigates the motion response of the platform under regular wave conditions without adopting an additional turbulence model. The numerical simulation directly solves the Navier–Stokes equations, in which momentum dissipation is realized through the fluid's molecular viscosity. The approach inherently captures nonlinear effects, flow separation, and viscous effects.

The Volume of Fluid (VOF) method is employed to capture air-water interface. An artificial parameter α is assigned to represent the volume fraction of the marked fluid in each grid cell. Based on this definition, the grid cells in the computational domain can be divided into three parts: the air region, the air-water interface, and the water region.

$$\frac{\partial \alpha}{\partial t} + \nabla \cdot (\boldsymbol{U}\alpha) = 0 \tag{4}$$

$$\begin{cases} \alpha = 0 & \text{air} \\ 1 < \alpha < 0 & \text{free surface} \\ \alpha = 1 & \text{water} \end{cases} \tag{5}$$

2.2. Wave generation

The relaxation zone wave generation method is employed for numerical wave generation. Within the designated wave-generation zone of the computational domain, a flow property ϕ (e.g., flow velocity $\boldsymbol{U}$ or volume fraction α) is defined as follows:

$$\phi = \gamma\phi_c + (1\text{-}\gamma)\phi_t \tag{6}$$

where γ is the relaxation factor, ϕ_c is the calculated value, ϕ_t is the target value.

2.3. Six-degree-of-freedom (6-DoF) motion

In the naoe-FOAM-SJTU solver, two sets of coordinate systems are defined for the floating platform motion problem: the earth-fixed inertial coordinate system and the body-fixed non-inertial coordinate system. Force and moment are solved in the earth-fixed coordinate system, and then converted to the body-fixed coordinate system through coordinate transformation methods to solve the six-degree-of-freedom motion equations.

$$\boldsymbol{F} = J_1^{-1} \cdot \boldsymbol{F}_e \tag{7}$$

$$\boldsymbol{M} = J_1^{-1} \cdot \boldsymbol{M}_e \tag{8}$$

where $\boldsymbol{F}$ and $\boldsymbol{M}$ is the forces and moments in the earth-fixed coordinate system, $\boldsymbol{F}_e$ and $\boldsymbol{M}_e$ is the forces and moments in the earth-fixed coordinate system, J_1^{-1} is the inverse of the transformation matrix.

2.4. Mooring system model

In the numerical simulation, a horizontal spring mooring scheme is adopted to maintain consistency with the model test. Based on the spring model, Hooke's Law is applied to calculate the mooring tension:

$$F = k \cdot \Delta l \tag{9}$$

where F is the mooring tension, directed from the mooring point to the anchor point; k is the spring stiffness; Δl is the spring deformation.

3. Numerical step and verification

3.1. Geometry

A new type of asymmetric CFPSO is used for computations in this paper. The model geometry and main particulars of the platform are shown in Fig. 3 and Table 1. It is worth noting that the heave plates in this CFPSO model have undergone special treatments. Different from the traditional complete circular heave plate, three “openings” are designed on the heave plate, dividing it into three parts. Among them, serrated protrusions are uniformly distributed on Plate 3; Plates 1 and 2 are mirror-symmetrical, while 1/3 of each plate has been subjected to “edge-cutting” treatment. Both the numerical simulations and model tests in this study were conducted at a 1:60 scale ratio, maintaining

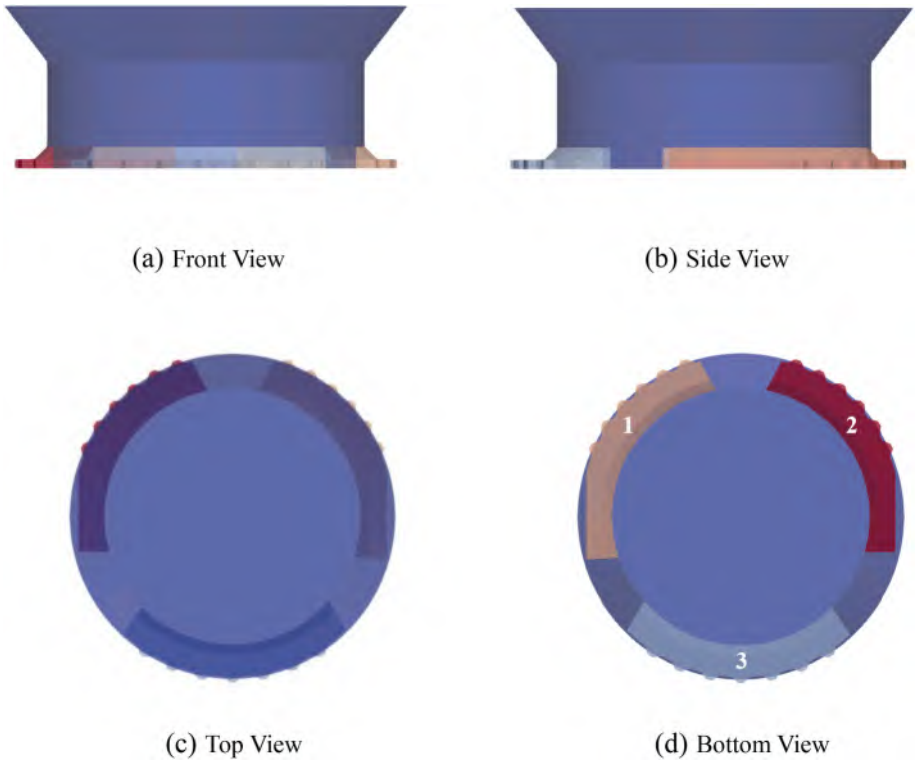

Fig. 3. Geometric model of the CFPSO with complex heave plates.

Table 1
Main parameters of the CFPSO model.

Parameter name	Unit	Full scale	Model scale
Ballast Draft	m	20	0.333
Displacement	t	132502 360	0.614
Height of CG Above the Baseline	m	21.4	0.356
Radius of Gyration in Roll	m	30.5	0.508
Radius of Gyration in Pitch	m	30.5	0.508
Radius of Gyration in Yaw	m	36.4	0.607 60
Hull diameter at waterline surface	m	110	1.833

kinematic and dynamic consistency based on Froude scaling lows. The opening distance between Plate 1 and Plate 2 is 17.16 m, and the spacing between Plate 2 and Plate 3 is 20.58 m. Both Plate 1 and Plate 2 are designed with combined edge-cutting profiles and serrated protrusions. The edge-cutting length is 29.5 m, and six serrated protrusions are arranged along the outer edge of the heave plate with a uniform spacing of 7.5 m. Seven serrated protrusions are evenly distributed on Plate 3 at an interval of 12.3 m. All serrated protrusions are identical, with a tooth height of 4.2 m and a protrusion angle of approximately 40°. To control variables and investigate the effects of special auxiliary structures attached to heave plates on motion responses, a series of six control groups were established in this study, namely: CFPSO with intact circular heave plates, CFPSO with openings heave plates, CFPSO with serrated protrusions heave plates, CFPSO with edge-cutting heave plates, CFPSO with openings and edge-cutting heave plates, and CFPSO with openings and serrated protrusions heave plates. Schematic diagrams of the control-group models are shown in Fig. 4.

To evaluate the influence of various wave-facing configurations on motion responses, the CFPSO was rotated while maintaining the mooring system layout constant in both numerical simulations and physical tank tests. Six configurations are considered in the present study,as shown in Fig. 5 and Table 2. Since the mooring systems of the six configurations are identical, and during the numerical calculation process, we controlled the moment of inertia and center of gravity position of the six models to be completely consistent by adjusting factors such as ballast position. The subsequent differences in motion and load generated during the regular wave motion analysis will be entirely attributed to the structural characteristic differences of the wave-facing heave plates.

3.2. Mooring configuration

The horizontal mooring system (HMS) was adopted in the tank test, and the relevant mooring parameters are listed in Table 3. The schematic diagram of the mooring arrangement is shown in Fig. 6, and the photograph of the test site is presented in Fig. 7.

To ensure the accuracy of the mooring system modeling, static displacement tests were performed for both numerical simulation and physical model test. The resulting displacement curves are presented in Fig. 8, which shows good agreement between numerical simulation and physical model test.

3.3. Computation domain

The computational domain is configured as illustrated in Fig. 9. The domain spans 30 m in length, 16 m in width, and 7.25 m in total height, with a water depth of 5.25 m. The platform is initially positioned at the origin (0, 0, 0). The wave generation zone is set in the range of (−10 m, −4 m) along the x-direction and the wave absorption zone is set in the range of (7 m, 20 m) along the x-direction.

3.4. Boundary conditions and numerical schemes

Regarding boundary conditions, *zeroGradient* is applied at the inlet, outlet, and bottom, while *symmetry* and *totalPressure* conditions are prescribed for the lateral sides and the top boundary, respectively. A no-slip condition is enforced on the hull surfaces. For temporal

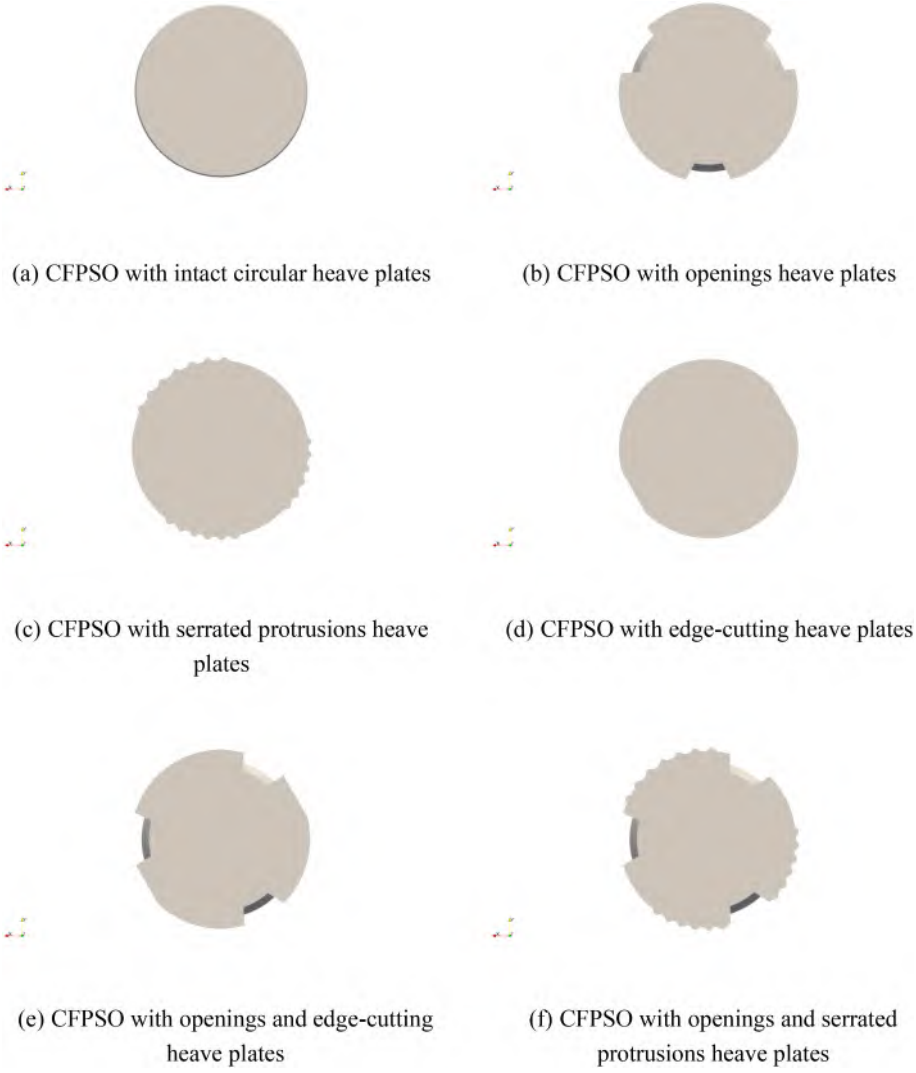

Fig. 4. The control-group CFPSO.

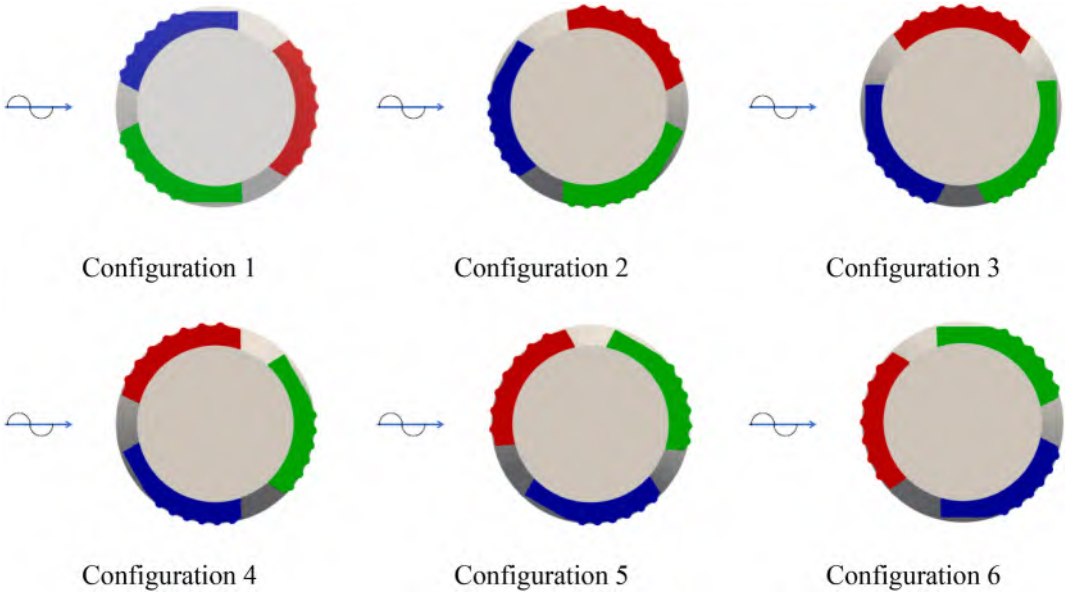

Fig. 5. Schematic diagram of different wave-facing structural characteristics.

Table 2
Summary table of different wave-facing configurations.

Numbering of setting	Edge-cutting	Serrated protrusions	Openings
Configuration 1			✓
Configuration 2	✓	✓	
Configuration 3	✓	✓	✓
Configuration 4	✓	✓	✓
Configuration 5		✓	✓
Configuration 6		✓	

Table 3
Horizontal mooring system Configuration.

Number		X (m)	Y (m)	Z (m)	Initial Length (m)	Stiffness (kN/m)
1	Anchor Point	31.08	−31.08	0	150	4464.9
	Fairlead	168.96	−168.96	0		
2	Anchor Point	31.08	31.08	0	150	4464.9
	Fairlead	168.96	168.96	0		
3	Anchor Point	−31.08	31.08	0	150	4464.9
	Fairlead	−168.96	168.96	0		
4	Anchor Point	−31.08	−31.08	0	150	4464.9
	Fairlead	−168.96	−168.96	0		

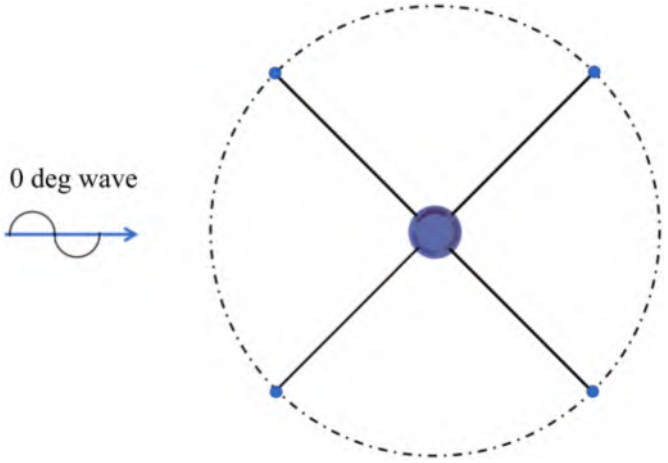

Fig. 6. Mooring system of the CFPSO.

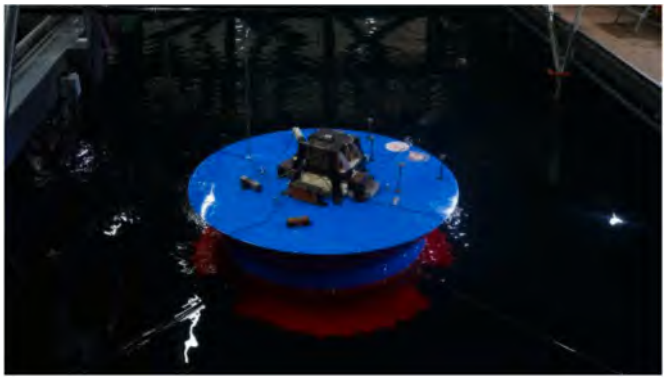

Fig. 7. Photograph of EXP mooring arrangement.

discretization, the Crank-Nicolson scheme is adopted with a blending coefficient of 0.95. Gradient terms are discretized using the *cellLimited*

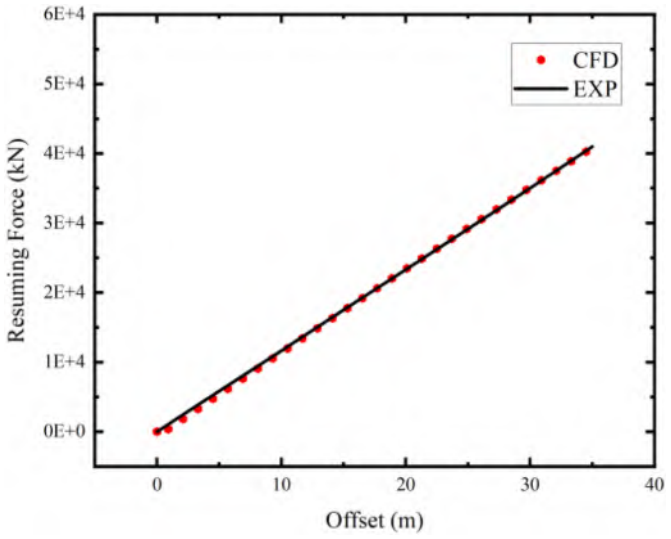

Fig. 8. Static displacement test results of horizontal mooring.

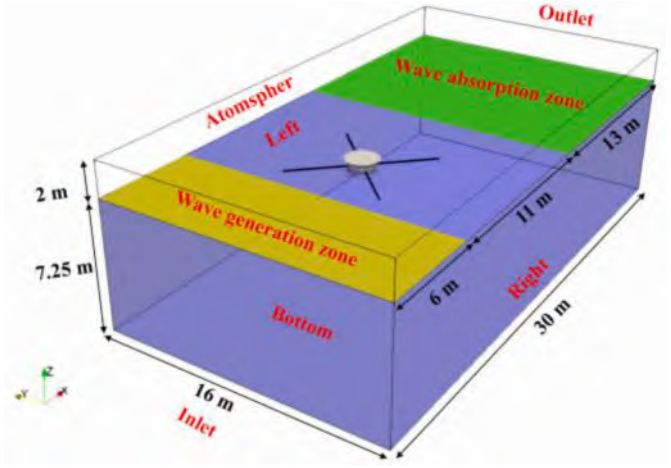

Fig. 9. Computation domain setting.

Gauss linear scheme with a limiter coefficient of 1. Covective terms are treated with a second-order linear upwind scheme. And the PIMPLE algorithm is employed to decouple the velocity and pressure fields.

3.5. Convergence study

To balance computational accuracy and computational cost, grid convergence analysis must be performed. Since we need to conduct regular wave calculations with the same wave height but different wave periods subsequently, and the range of periods we need to consider is relatively wide, it is necessary to design different grids for different wave periods. To save space, grid convergence analysis is performed herein for the full-scale working condition with a wave period of $T = 16$ s and a wave height of $H = 3$ m. Based on empirical methods, three sets of grids with different quantities were designed for grid convergence verification and analysis. The main difference among the three sets of grids lies in the number of grids within one wavelength and the number of grids within one wave height, as detailed in Table 4 below. N_{total} represents the total number of grids, $\frac{H}{\triangle z}$ denotes the number of grids within one wave height, and $\frac{\lambda}{\triangle x}$ denotes the number of grids within one wavelength. The convergence was judged by comparing the time series curves of the Configuration 4, and the results are shown in Fig. 10 below. As can be seen from the results in Fig. 10, the calculation results of the coarse grid

Table 4
Grid parameters in mesh convergency study.

Mesh	N_{total}	$\frac{H}{\triangle z}$	$\frac{\lambda}{\triangle x}$
Coarse	1.48M	6	77
Medium	5.30M	13	154
Dense	7.90M	13	220

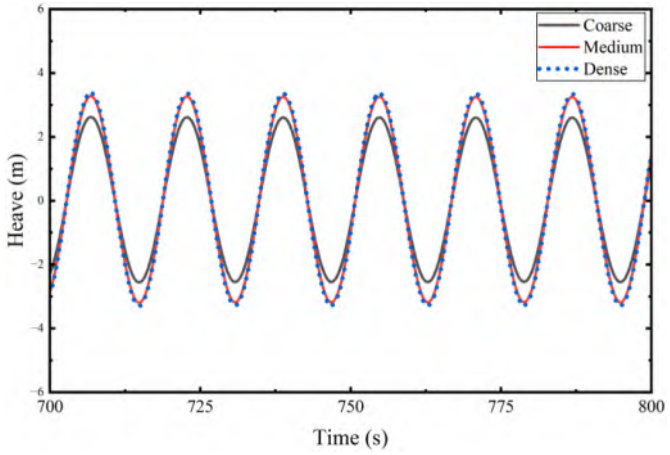

Fig. 10. Time series curves of platform motion with different mesh settings.

are significantly smaller than those of the other two sets of grids, and the differences between the results of the medium-density grid and the dense grid are extremely small. Therefore, the medium-density grid configuration will be adopted in subsequent studies, with the grid details shown in Fig. 11 below.

A time-step sensitivity study was also conducted. Three distinct time-step sizes were evaluated, with the heave motion response serving as the primary metric for convergence, as illustrated in Fig. 12. Based on these results, a time step of $\Delta t = 0.005$ s was selected for the subsequent simulations. Throughout the simulation, the maximum Courant number was less than 1, ensuring numerical stability.

3.6. Case condition

To validate the numerical model, regular wave simulations were performed under conditions consistent with those utilized in the

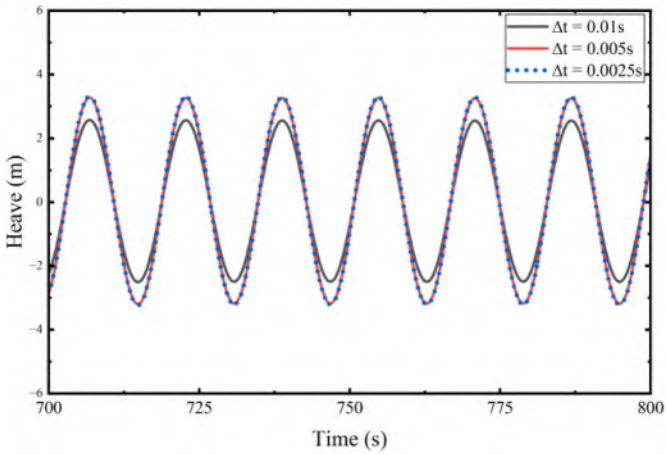

Fig. 12. Time series curves of platform motion under medium-density grid settings with different time steps.

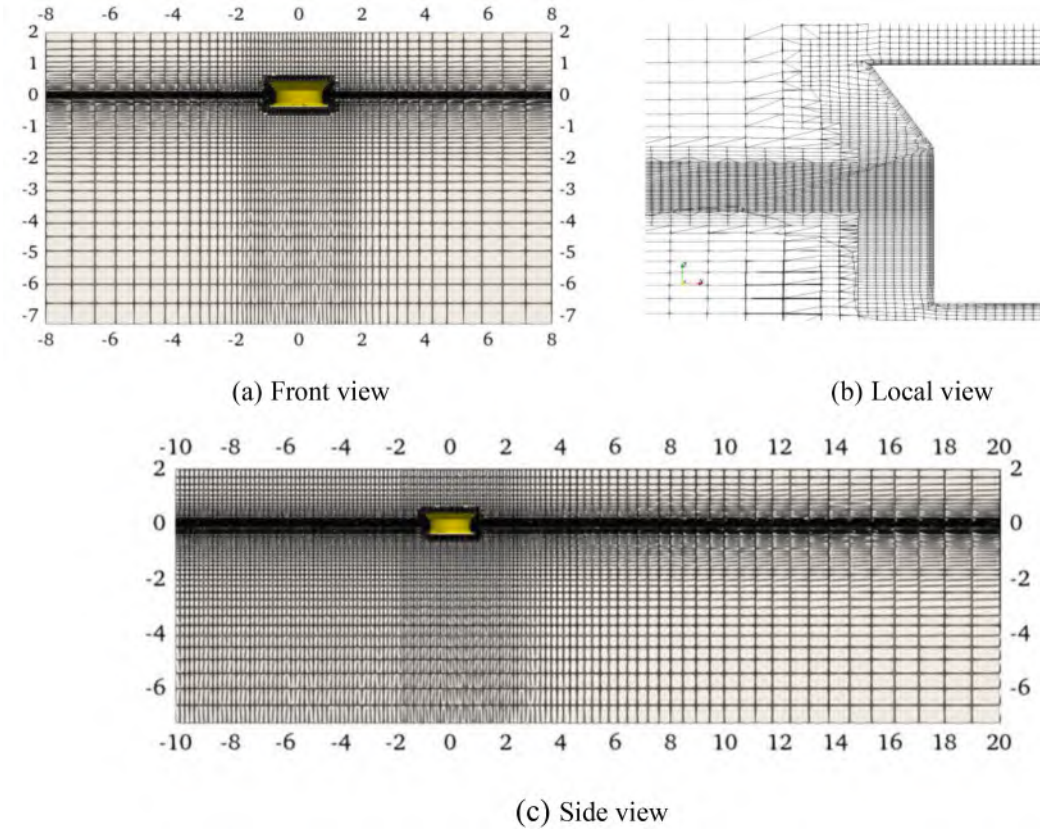

Fig. 11. Computational mesh.

physical model tests. The specific wave parameters employed in these computational cases are summarized in Table 5.

3.7. Validation

The validation work is divided into two parts. The first part investigates the influence of turbulence models on motion results, and the second part compares numerical simulation results with basin experimental data for validation.

Turbulence models mainly affect the damping characteristics of heave plates. Therefore, numerical simulations with different turbulence models are carried out for Configuration 4 of the CFPSO fitted with composite heave plates, and the obtained results are compared and analyzed. It can be observed that the present calculation results are in good agreement with those predicted by the k-ω SST model, while the LES model over predicts the damping level (see Fig. 13).

The second part of validation is completed by comparison with experimental test data. The model test was conducted in the tank laboratory of Shanghai Jiao Tong University, and a uniform scale ratio of 1:60 was adopted for both the test and numerical simulation. The accuracy of the numerical simulation method is validated by comparing the measured motion response results of Configuration 2, Configuration 4 and Configuration 6 under a series of regular waves from the tank test with those obtained from numerical simulation. Due to the large number of calculation cases, only the results of motion response amplitudes are presented herein to save space. The same numerical processing is performed on the original model test data and the numerical simulation data. The results comparison is shown in Fig. 14 below. Fig. 14 shows that the numerical simulation results obtained with the aforementioned numerical settings exhibit high accuracy in both trend and magnitude compared with those derived from the model test.

4. Results and discussions

In this paper, since the wave incidence direction is consistently 0°and the layout of the mooring system is symmetric with respect to this direction, the main motions of the platform occur in the surge, heave, and pitch degrees of freedom (DOFs). Subsequently, the influence of structural differences in the wave-facing heave plates on motion performance will be analyzed separately from the time domain and frequency domain.

4.1. Free decay

To better understand the motion characteristics of the CFPSO, free decay calculations for heave and pitch of Configuration 4 without a mooring system are first performed. The free decay calculation for surge is not performed, as its natural period is generally large, far from the wave period range, and significantly influenced by the stiffness of the mooring system. Free decay is implemented by applying initial forced displacements and rotations, the results presented in Fig. 15. It can be seen from the results that the heave free decay period is approximately 16 s, and the pitch free decay period is about 27 s. From the free decay

Table 5
Wave condition design.

Case	Wave height (m)	Wave period (s)
1	3	7
2	3	9
3	3	10
4	3	12
5	3	14
6	3	15
7	3	16
8	3	18
9	3	20

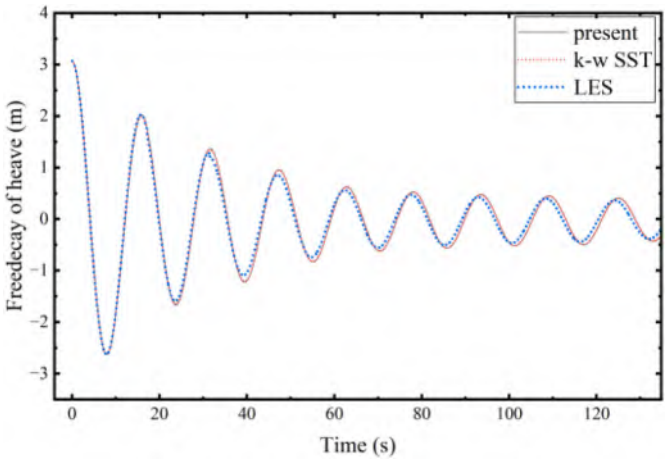

Fig. 13. Comparison of different turbulence models.

time-history curves, the numerical calculations are in high agreement with the experiment for pitch, while there is a certain error for heave. The free decay periods are calculated by taking the first five cycles, with an error of approximately 1%. Calculated from the free decay curves, the heave damping ratio of the platform is approximately 5.07%, and the pitch damping ratio is about 3.80%.

4.2. Wave motion response for CFPSOs with different heave plate

This paper compares the CFPSO with complex heave plates with the other six CFPSOs under same wave conditions to verify that complex heave plates deliver superior performance. As can be seen from the free decay results in Section 4.1, the natural period of heave is approximately 16 s, which falls within the full range of wave periods analyzed. Therefore, this paper selects the working condition with a heave natural period of 16 s and wave height of 3 m for comparative research. To better analyze the time-history motion results, we perform decomposition processing on the time-history curves via filtering. Taking the calculated results of the stable segment of Configuration 1 equipped with complex heave plates as an example, the time-history motion curves are decomposed into first-order wave-frequency motion and low-frequency motion by filtering, and the decomposition results are shown in Fig. 16. The CFPSO fitted with complex heave plates and the other six CFPSOs are processed by adopting the same aforementioned method, and the corresponding results are presented in the following Table 6. In Table 6, "+" indicates that the motion response is larger than that of the intact circular heave plate, and "-" means the motion response is reduced. The first-order wave-frequency surge refers to the periodic motion around the equilibrium position induced by first-order wave forces, and the definitions of the other two degrees of freedom follow the same rule. Low-frequency surge motion refers to the surge displacement induced by the characteristics of the mooring system, whereas slow-drift motion is generated by mean drift forces.

As shown in Table 6, the sole addition of opening structures can effectively reduce the first-order pitch motion, low-frequency surge motion and slow-drift responses, yet significantly amplify the first-order heave motion. Independently arranging serrated protrusions mainly suppresses first-order heave motion but results in a remarkable rise in slow-drift motion. In comparison, the separate use of edge-cutting structures has a slight impact on all platform motions and only marginally aggravates heave motion. When edge-cutting treatment is added to the opening-equipped heave plate, the first-order heave motion is further amplified, while the suppression effect on low-frequency surge motion is greatly enhanced. Arranging serrated protrusions on the original opening heave plate can effectively offset the amplification of heave motion induced by openings, though slow-drift responses remain

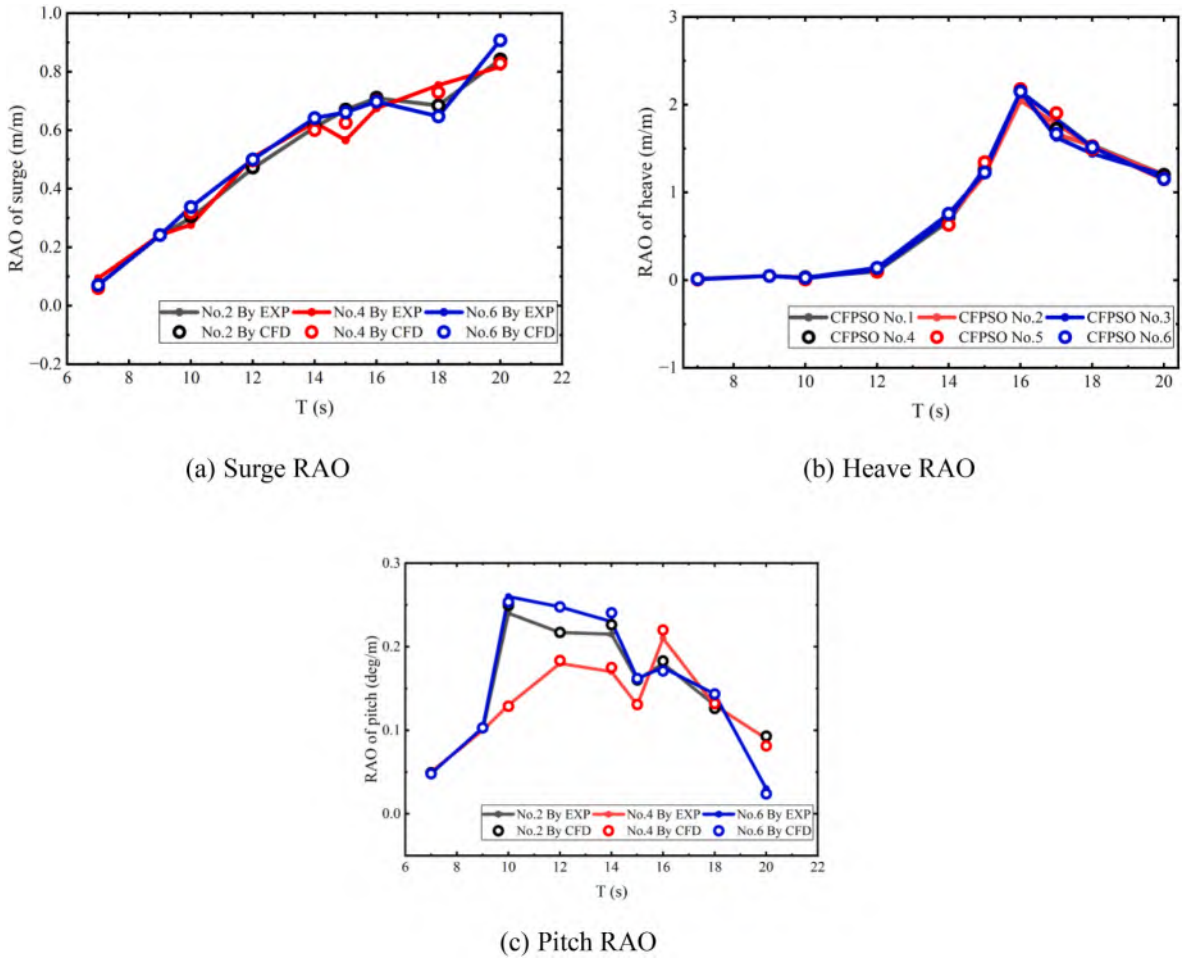

Fig. 14. RAO of the Configuration 2, Configuration 4 and Configuration 6 by CFD and model test.

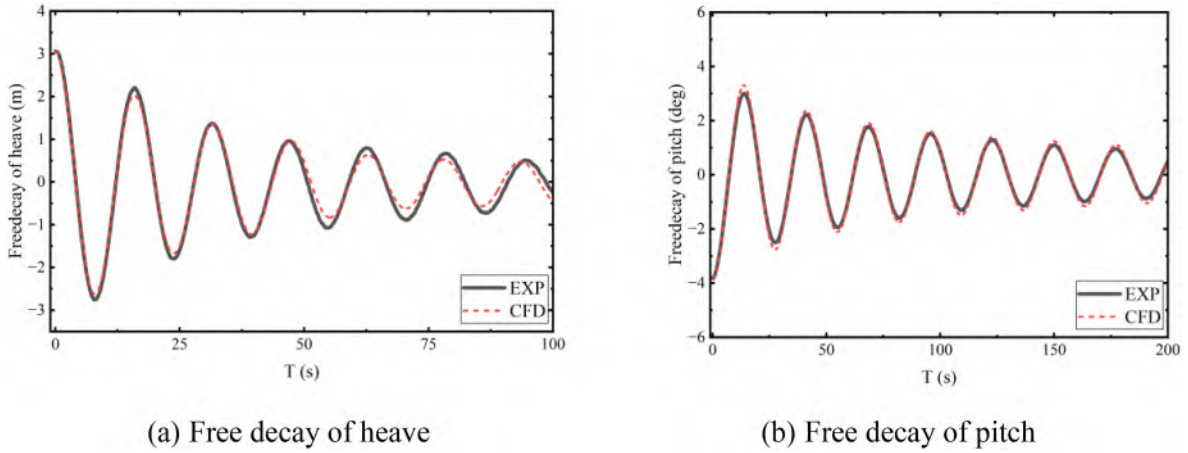

Fig. 15. Free decay of the Configuration 4 by CFD and experiment.

obviously increased. Ultimately, the complex heave plate integrated with openings, edge-cutting and serrated protrusions not only exerts favorable suppression on first-order pitch motion, low-frequency surge motion and slow-drift responses derived from openings and edge-cutting, but also maintains stable performance of first-order heave motion.

4.3. Wave motion response for different wave-facing configuration

Based on previous research, complex heave plates have been proven to significantly improve the motion performance of CFPSO. To further investigate the effect of wave-facing configurations on platform motion characteristics, numerical simulations are conducted for the six wave-facing configuration layouts introduced above. Using the same method, the motion results of Platforms Configuration 1 to Configuration 6 under Wave Condition 8 are filtered, and the processed results are

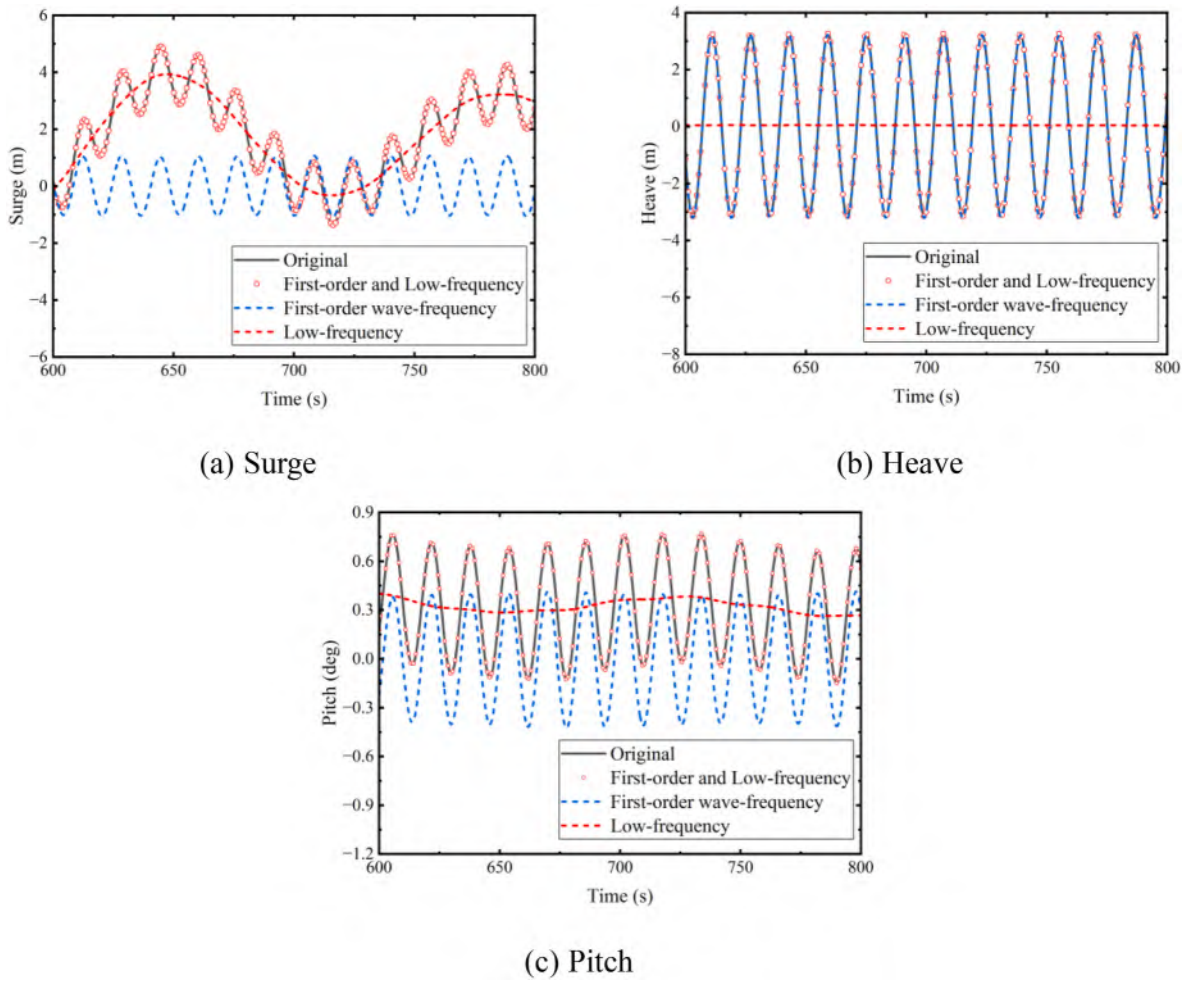

Fig. 16. Original time-history data and filtered results.

Table 6
Motion results of seven CFPSOs with different heave plates.

heave plate characteristics	first-order wave-frequency surge (m)	first-order wave-frequency heave (m)	first-order wave-frequency pitch (deg)	low frequency surge (m)	slow-drift motion (m)
intact circular	0.696	1.649	0.292	2.479	1.754
openings	0.688	2.018	0.260	1.760	0.995
	−1.15%	+22.34%	−10.96%	−28.98%	−43.28%
serrated protrusions	0.680	1.335	0.280	2.712	1.924
	−2.41%	−19.04%	−4.11%	+9.42%	+9.70%
edge-cutting	0.698	1.722	0.279	2.428	1.805
	+0.23%	+4.39%	−4.45%	−2.03%	+2.94%
openings and edge-cutting	0.698	2.076	0.270	1.414	1.144
	+0.29%	+25.90%	−7.53%	−42.94%	−34.76%
openings and serrated protrusions	0.685	1.534	0.267	1.951	1.888
	−1.61%	−6.99%	−8.56%	−21.27%	7.66%
complex	0.690	1.645	0.251	1.586	1.352
	−0.86%	−0.25%	−14.04%	−36.03%	−22.92%

summarized in Figs. 17 and 18 below. To present the results more clearly, only the results from 600 to 650 s are shown for the first-order motions, while the results from 600 to 800 s are displayed for the high-order motions. In the legend, the six types of models are identified using different colors and line types, with a total of three colors and two line types adopted. The same color indicates similar structures facing the wave incidence. For example, black represents structures with openings (Configuration 1 and Configuration 4), red represents integral heave plates (Configuration 2 and Configuration 6), and blue represents combinations of openings and other forms (Configuration 3 and Configuration 5). Different line types denote the presence or absence of edge-cutting.

Fig. 17 indicate that the shapes of the heave plates of CFPSOs with different wave-facing sides have little influence on the first-order surge and heave, but mainly affect the first-order pitch. It is found that this result is highly correlated with the structural shape characteristics facing the waves—specifically, as the opening gradually deviates from the wave incidence angle, the pitch motion amplitude decreases

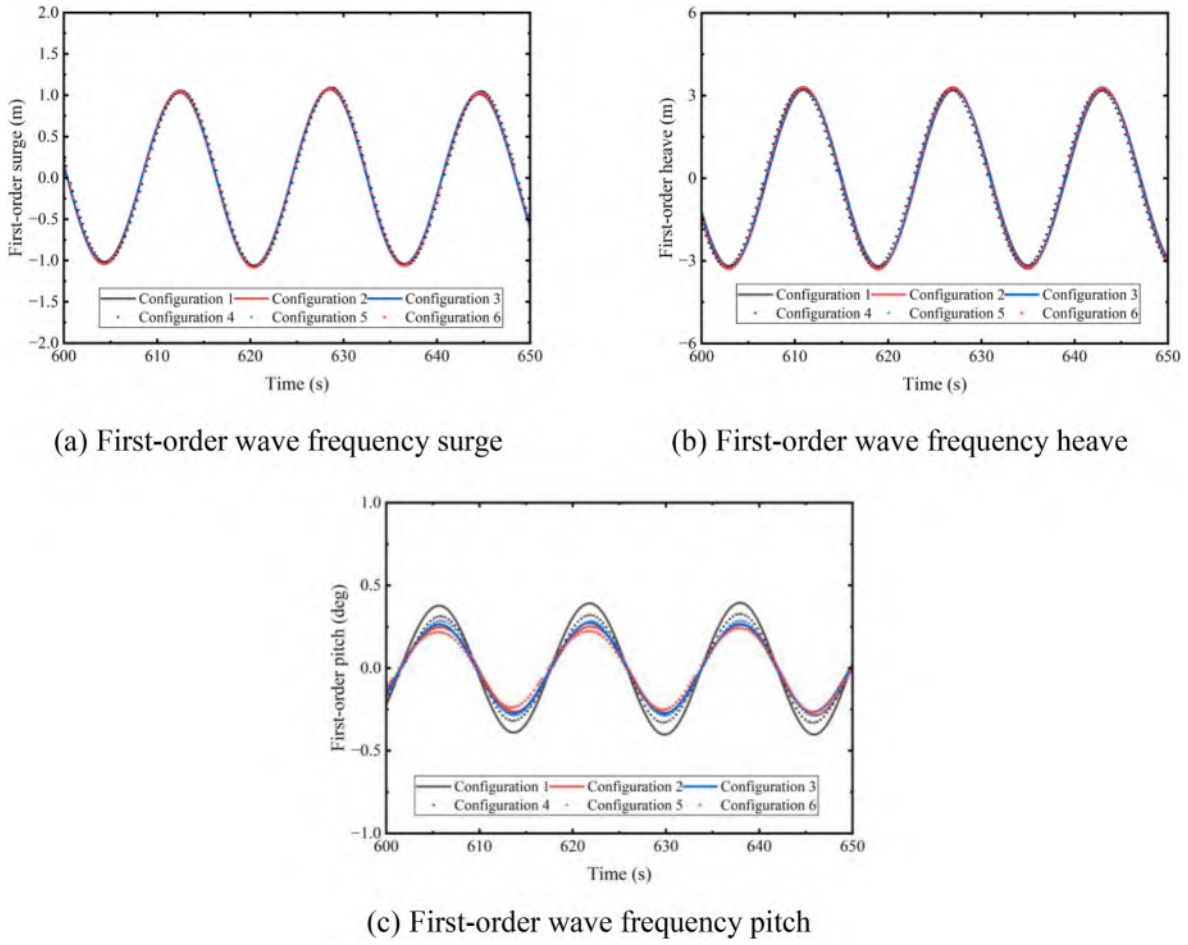

Fig. 17. First-order wave frequency CFPSO motion result.

progressively. When the structure facing the waves is an opening (Configuration 1), the pitch motion is the most significant with an amplitude of 0.47 deg, which is approximately 51% larger than the pitch motion amplitude of 0.31 deg for the integral heave plate (Configuration 2).

In addition, by comparing models with the same relative position between the opening and the waves, it can be found that the impact of edge-cutting treatment on the heave plate of pitch motion is significant. In addition, a comparison of models with identical relative positions between openings and incident waves reveals that adding edge-cutting treatment to the wave-facing side of the heave plate exerts a noticeable effect on pitch motion. For instance, the core distinction between Configuration 1 and Configuration 4, Configuration 2 and Configuration 6, as well as Configuration 3 and Configuration 5 lies in whether edge-cutting is adopted on the wave-facing side. When openings directly face incoming waves, edge-cutting reduces the pitch amplitude by approximately 20%, whereas only a 3% reduction is achieved if the openings deviate from the wave incidence direction.

Fig. 18 shows that the differences in the structural characteristics of the wave-facing heave plates have a more significant impact on low-frequency motions than on first-order wave-frequency motions. The low-frequency surge coupled with the mooring system and slow-drift motions are counted separately, and the statistical results are summarized in Table 7 below.

Table 7 shows that the surge motions of Configuration 2 and 6 are significantly larger than those of the other four models. It can thus be concluded that when the integral heave plate is directly facing the wave incidence, the surge motion increases significantly. In addition, edge-cutting reduces the surge motion of Configuration 2 by 4.8% compared with Configuration 6, and that of Configuration 4 by 19.4% compared with Configuration 1. Compared with the 4.8% inhibition effect in the former case, this amplified inhibition effect reappears when edge-cutting is applied to the opening directly facing the waves, which is consistent with the law observed in the first-order pitch motion. The results of the slow-drift motions are consistent with the trend of the previous surge motions. When the integral heave plate is directly facing the wave incidence, the slow-drift motion is the most significant; edge-cutting can still effectively suppress the slow-drift motion, and this suppression effect is most obvious when the opening is directly facing the wave incidence. Fig. 18(c) shows that as the opening gradually deviates from the wave incidence direction, the low-frequency pitch motion is gradually suppressed, which is consistent with the overall law of the first-order pitch motion. Comparing the results of Configuration 1 and Configuration 4, it can be seen that when the opening is directly facing the waves, the inhibitory effect of edge-cutting is very significant.

Based on the above research results, the following conclusions can be drawn: First, the influence of different wave-facing attitudes of the CFPSO equipped with complex heave plates on the platform motion characteristics is mainly concentrated in the low-frequency slow-drift motion, low-frequency pitch motion and first-order pitch motion; Second, for the CFPSO fitted with composite heave plates, the edge-cut structure exerts an evident influence on platform motions. When the combined structure of edge-cut and openings faces the incident wave direction head-on, the suppression performance is greatly enhanced, which demonstrates a prominent coupling effect between the two structural forms.

The subsequent three subsections combine detailed flow field characteristics to deeply analyze the influence characteristics of different

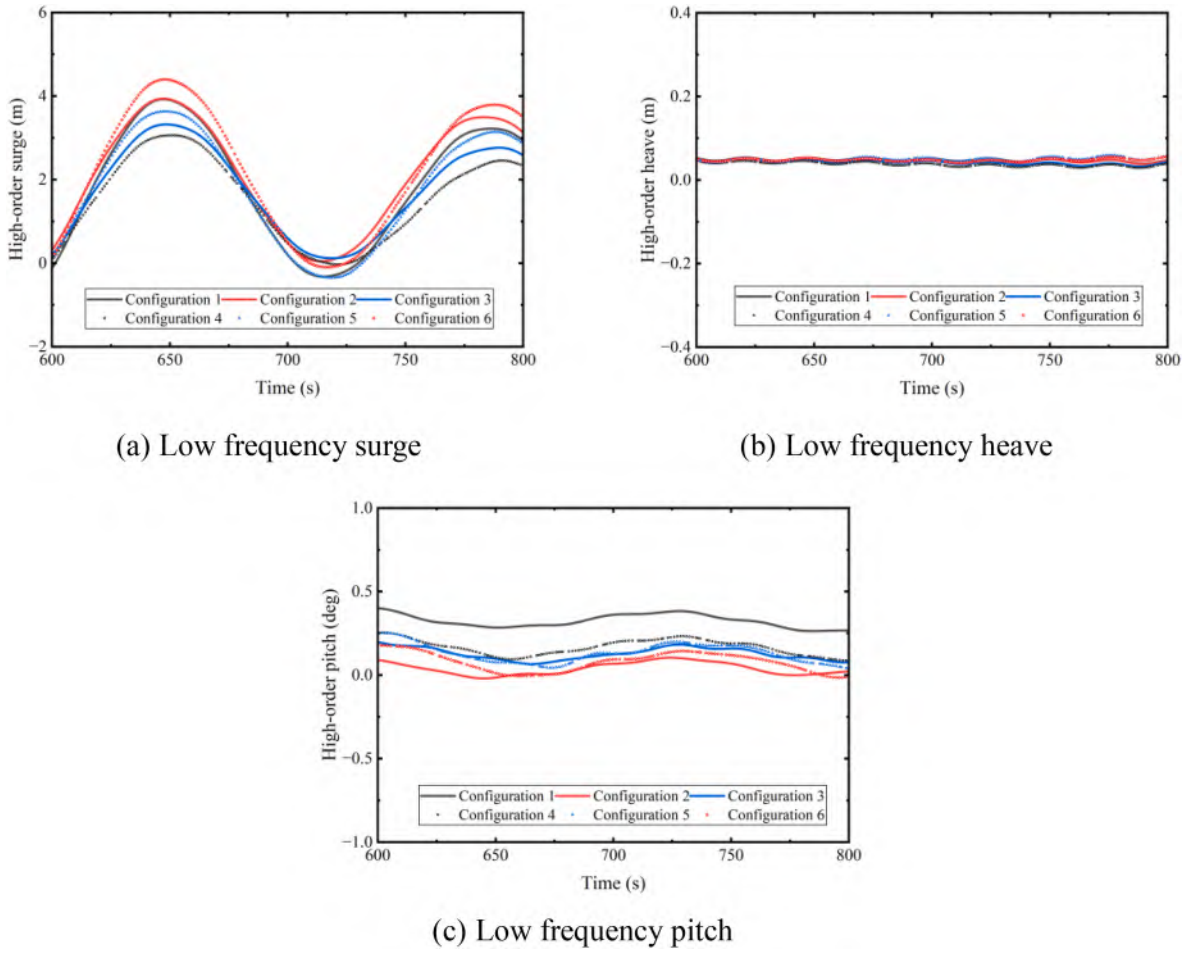

Fig. 18. Low frequency CFPSO motion result.

Table 7
Low frequency motion result.

Model	Configuration1	Configuration2	Configuration3	Configuration4	Configuration5	Configuration6
low frequency surge (m)	1.60	1.86	1.56	1.34	1.53	1.95
slow-drift motion (m)	1.98	2.05	1.56	1.50	1.93	2.20

wave-facing heave plate structures on platform motion, and sequentially clarify the variation characteristics of slow drift, the effect of edge-cutting structure, and the variation characteristics of pitch motion.

4.4. Slow-drift characteristics

Based on the previous summary and collation of the structural characteristics, Configuration 1, Configuration 5, and Configuration 6 are not affected by edge-cutting, and their openings are gradually far away from the wave incident direction. Therefore, the flow field results calculated for Configuration 1, Configuration 5 and Configuration 6 under the working condition of wave period $T = 16$ s are sliced to obtain the flow field distribution in the XoZ plane, as shown in Fig. 19 below. Presented here is the flow field distribution state within a complete wave period in the stable phase. Specifically, the platform is at the equilibrium position at time t, reaches the highest point of motion within the period at t + 0.25T, returns to the equilibrium position at t + 0.5T, reaches the lowest point of motion within the period at t + 0.75T, and returns to the equilibrium position again at t + T.

The results in Fig. 19(a) show that when the CFPSO Configuration 1 moves upward, due to viscous effects, a fluid with a relatively large positive horizontal velocity is generated at the bottom of the wave-facing side of the heave plate (near the opening structure). As the platform moves upward, this part of the fluid gradually detaches, continuously dissipates energy, and is eventually assimilated by the surrounding fluid. Meanwhile, a new fluid with negative horizontal velocity is generated at the bottom of the platform. During the platform's fall back to the equilibrium position, this part of the fluid further develops and partially spreads to the front of the platform. As the platform moves downward from the highest point, this part of the fluid with negative horizontal velocity also dissipates rapidly. When the CFPSO starts moving upward again from the lowest point of its motion, the high-velocity fluid with positive velocity reappears below the heave plate. Similar fluids are also generated on both the upper and lower sides of the heave plate on the leeward side of Configuration 1, but the influence range and intensity of these fluids are significantly smaller than those of the fluids on the wave-facing side.

Fig. 19(b) and (c) show the distribution characteristics of the horizontal flow field around the CFPSO when the wave-facing structure is a heave plate. For Configuration 5, the slicing position is located at the concave of the serrated structure; while for Configuration 6, the slicing position is located at the convex of the serrated structure. Thus, the

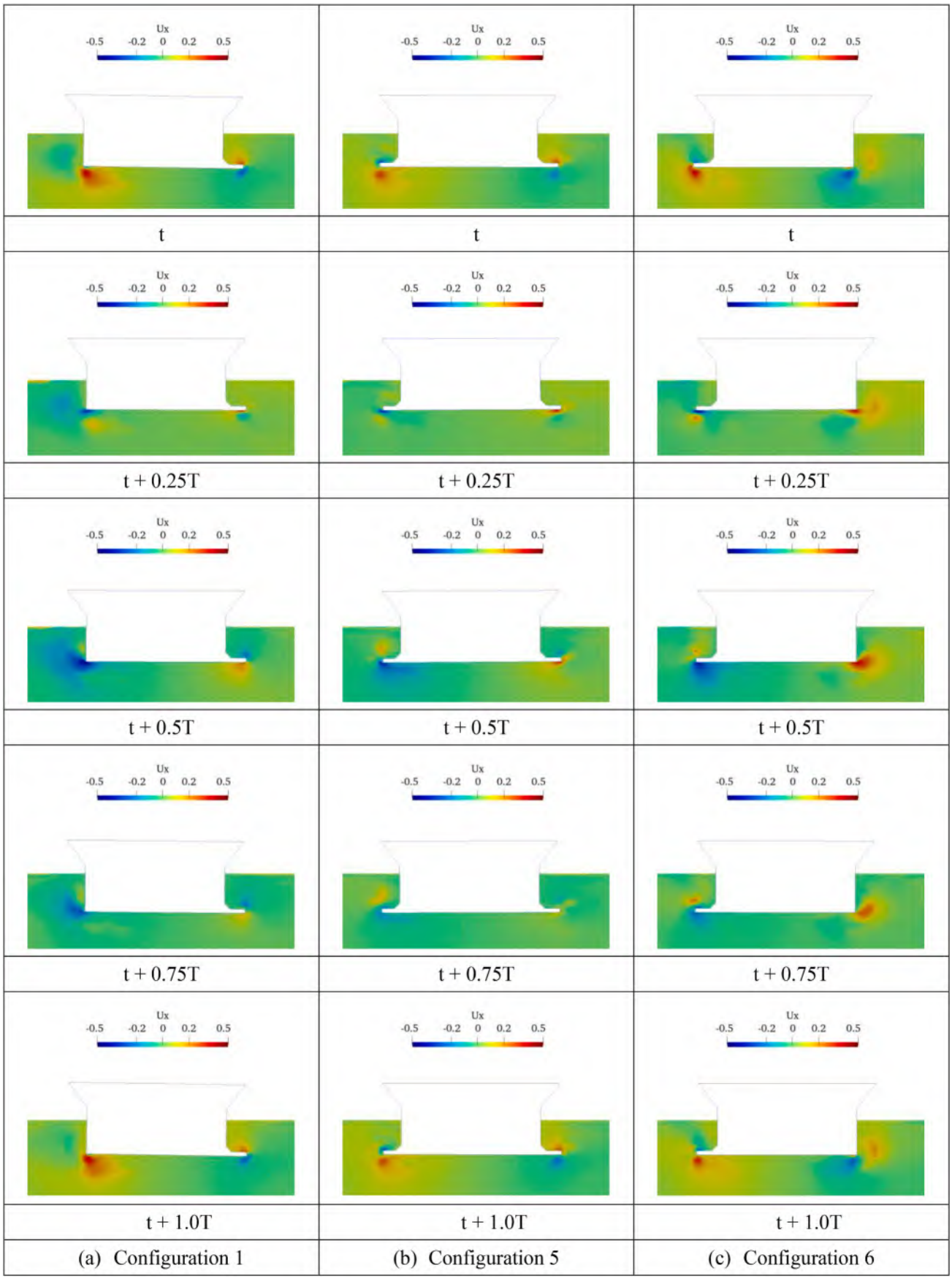

Fig. 19. Horizontal flow field around Configuration 1, Configuration 5, Configuration 6 in XoZ plane.

length of the heave plate on the left side in the two figures is different. The results indicate that two parts of fluid with opposite horizontal velocities are generated on both the upper and lower sides of the heave plate of the CFPSO.

First, the flow field characteristics on the lower side of the heave plate are analyzed: the variation law of the fluid in this region is similar to that shown in Fig. 19 (a). As the CFPSO moves upward, the fluid velocity gradually dissipates and is assimilated by the surrounding fluid; at the same time, new fluid clusters with opposite velocities are continuously generated on the lower side of the heave plate, and the motion intensity of these fluid clusters gradually increases. Different from the results of Configuration 1 at the same time step, owing to the outward extension of the heave plate by a certain distance, these fluid clusters with opposite velocities basically do not spread to the front of the CFPSO but dissipate gradually. It can be clearly observed that the fluid clusters at the bottom of Configuration 5 dissipate rapidly, while those at the bottom of Configuration 6 persist for a relatively long time. When Configuration 6 moves upward again, the fluid clusters with positive velocity generated at its bottom are comparable to those of Configuration 1 at the same moment in terms of intensity, volume and influence range, whereas the fluid clusters of Configuration 5 are significantly weaker than those of Configuration 1 and Configuration 6. In addition, it can be clearly observed that on the leeward side of Configuration 6, the absence of an extended section of the heave plate to block the upward diffusion of vortices results in a significant influence, a phenomenon that has not been observed in the flow fields of Configuration 1 and Configuration 5.When Configuration 6 moves upward again, the fluid clusters with positive velocity generated at its bottom are comparable to those of Configuration 1 at the same moment in terms of intensity, volume and influence range, whereas the fluid clusters of Configuration 5 are significantly weaker than those of Configuration 1 and Configuration 6. In addition, it can be clearly observed that on the leeward side of Configuration 6, the absence of an extended section of the heave plate to block the upward diffusion of vortices results in a significant influence, a significant influence that has not been observed in the flow fields of Configuration 1 and Configuration 5.

Secondly, an analysis is conducted on the flow field characteristics on the upper side of the heave plate. Reviewing the results in Fig. 19 (a), it can be seen that when the wave-facing structure is an opening, almost no obvious distribution of fluid clusters is observed in the area above the wave-facing heave plate excited by the platform motion, with only a partial influence diffused from the lower side of the heave plate. However, for Configuration 5 and Configuration 6, the fluid with opposite velocities on the upper side of the heave plate gradually dissipates as the platform moves upward, while the influence of this fluid on the entire flow field above the heave plate can still be detected. When the CFPSO starts to fall back from the highest point of its motion, high-velocity fluid with positive horizontal velocity is generated on the upper side of the heave plate, which further exerts an effect on the flow field above the heave plate. Among them, the fluid clusters generated on the upper side of the heave plate of Configuration 6 feature higher velocity, larger volume, more significant influence and wider action range, whereas the fluid clusters formed by Configuration 5 dissipate rapidly.

Based on the above flow field details, the reason why Configuration 5 performs slightly better than Configuration 1 and significantly better than Configuration 6 in low-frequency surge motion can be explained. Although the sliced sections of Configuration 5 and Configuration 6 are located at the concave and convex of the serrated structure respectively, their slice shapes are both rectangular with only a slight difference in length, which is insufficient to explain the significant discrepancy in the flow field distribution on the wave-facing side of the two devices. This study speculates that the reason for this phenomenon is that the wave-facing side of Configuration 5 does not adopt a complete serrated heave plate structure; in other words, it arises from the influence of the flow field surrounding the plane where the heave plate is situated.

Therefore, slicing processing is performed on the flow field around the heave plate to observe more flow details. Fig. 20 show the horizontal flow field distributions around the heave plates during the movement of Configuration 1, Configuration 5, and Configuration 6, respectively. All flow field results are in the plane where the central height of the heave plate is located.

Fig. 20(a) shows that when the wave-facing structure is an opening, the fluid with opposite velocity formed by the blocking effect of the CFPSO on the fluid is mainly distributed on the serrated heave plates on both sides deviated from the wave incident angle. This indicates that when the wave propagates near Configuration 1, it first contacts and interacts with the serrated heave plates on both sides, resulting in a significant reduction in the wave influence on the opening position facing the wave. In addition, since Configuration 1 is completely symmetric with respect to the wave incident direction, the projections of the thrust forces acting on the serrated heave plates on both sides of the opening onto the y-direction will be almost offset, leading to an extremely small roll motion of the platform.

Since both Configuration 6 and Configuration 1 are structurally symmetric with respect to the wave incident direction, Configuration6 is analyzed before Configuration5. Fig. 20(c) shows that during the contact process between Configuration 6 and the wave, the serrated heave plate directly facing the wave incidence is affected first, and an obvious fluid blocking area is formed at the front end of the serrated heave plate. The blocking area refers to the fluid region formed in front of the CFPSO, where the flow possesses an obvious reverse velocity or a velocity evidently lower than the average flow velocity of the surrounding fluid. Different from the periodic appearance and disappearance of the fluid blocking area near the opening of Configuration 1, the fluid blocking area at the front end of Configuration 6 exists throughout the entire wave period, and both the maximum fluid velocity and distribution area of the blocking area are significantly larger than those of the flow field around Configuration 1. In addition, the thrust generated by the small-scale fluid blocking areas distributed on the serrated heave plates on both sides of Configuration 1 only contributes partial components when projected onto the x-axis. In contrast, the thrust generated by the fluid blocking area at the front end of Configuration 6 has an extremely small component on the y-axis, which, from the perspective of motion, almost only affects the surge RAO and slow-drift motion. The surge RAO is mainly affected by the amplitude of the horizontal load, while the slow-drift motion is mainly affected by the mean value of the horizontal load. Therefore, a comparison between Fig. 20(a) and (c) can already explain why the slow-drift motion generated when the wave-facing side of the CFPSO is a complete serrated heave plate is significantly larger than that generated when the wave-facing side is an opening.

Fig. 20(b) presents the flow field distribution results around the heave plate of CFPSO Configuration 5 within half a wave period. Different from the structural symmetry of Configuration 1 and Configuration 6 with respect to the wave incident direction mentioned earlier, Configuration 5 has its wave-facing side directly aligned with the serrated heave plate, while an opening is located adjacent to this plate in the clockwise direction. Driven by the effect of the serrated heave plate, an obvious fluid blocking region is also formed at the leading edge of Configuration 5, but this region is generally biased toward the lower-left direction. In addition, due to the presence of the opening on the upper-right side, a large amount of accelerated fluid generated near the opening interferes with the flow field that would otherwise form a blocking region, resulting in a significant difference in the flow field distribution characteristics near the serrated heave plate between Configuration 5 and Configuration 6. The flow field characteristics near the opening are similar to those of Configuration 1, both alternating with the wave period, whereas the fluid blocking region near the serrated heave plate on the lower-left side persists almost throughout the entire wave period. This result also verifies the previous speculation regarding the flow field distribution differences between Fig. 19(b) and (c)—the cause of such differences lies not in the variation of the edge-cutting length of the heave plate, but in the influence of the opening

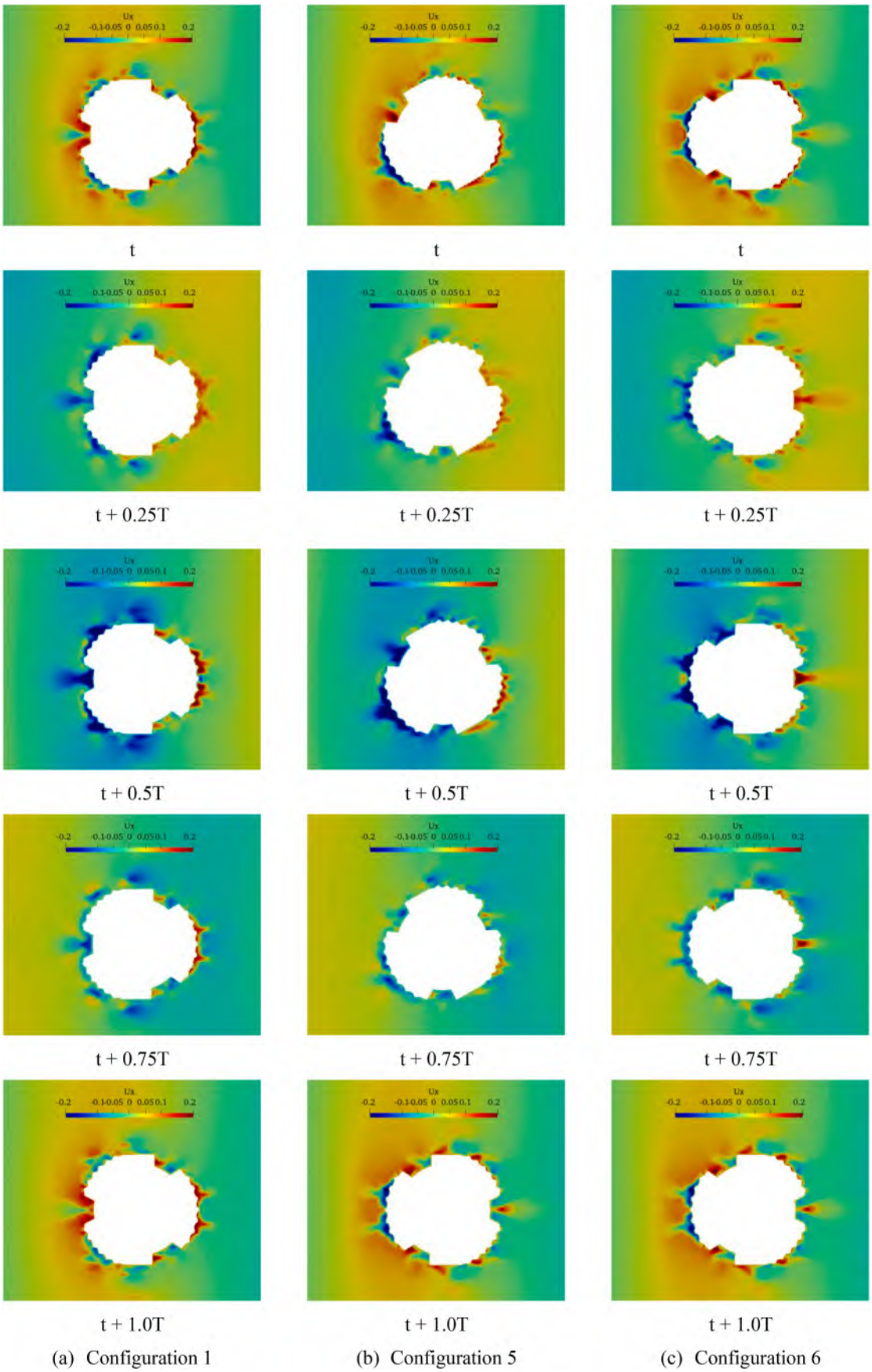

Fig. 20. Horizontal flow field around heave plate of Configuration 1, Configuration 5, Configuration 6.

structure of Configuration 5 on the flow field around the heave plate.

Under pure wave conditions, the fluid loads acting on the CFPSO are dominated by the pressure term. Therefore, the dynamic pressure distribution contours are supplemented in Fig. 21. It can be seen from the dynamic pressure cloud maps at the moment of t+0.5T in Fig. 21 that the magnitude of dynamic pressure near the heave plates of Configuration 1, Configuration 5 and Configuration 6 shows no significant difference. Nevertheless, affected by the difference in dynamic pressure distribution, the surge component of fluid pressure on Configuration 5 is smaller than that on Configuration 1, while its sway component is obviously larger. This analytical conclusion is further verified by the subsequent motion response results.

4.5. Edge-cutting effects

As can be seen from the aforementioned motion time-history curves, edge-cutting treatment exerts an inhibitory effect on the platform motion, and this inhibitory effect is significantly enhanced when the opening is directly aligned with the wave incident direction. In this work, Configuration 1 & Configuration 4 and Configuration 2 & Configuration 6 are selected for in-depth analysis of their flow fields under the edge-cutting condition. Among these cases, the flow field analysis results of Configuration 1 & 6 are presented in Fig. 19(a)–(c), Fig. 20(a) and (c); the flow details of Configuration 2 & 4 in the XoZ plane are shown in Fig. 22 below.

The Configuration 2 and Configuration 4 on the XoZ plane slices are exactly consistent with those of Configuration 6 and Configuration 1. Although the overall characteristics of the flow field distribution around each CFPSO are similar, there are significant differences in terms of the peak fluid velocity and its influence range. By comparing Figs. 19(a) and 22(b), it can be observed that the fluid vortices formed at the leading edge of Configuration 4 are significantly smaller than those of Configuration 1 in both peak velocity and volume distribution; especially in the latter half of the wave period, the area of the low-velocity blocking region at the leading edge of Configuration 4 is much smaller than that of the corresponding region at the leading edge of Configuration 1. It can be seen from Figs. 19(c) and 22(a) that although the flow field distribution around Configuration 2 also shows an optimization trend compared with that of Configuration 6, the magnitude of the change is relatively small. Based on the above analysis, a preliminary conclusion is drawn that the edge-cutting treatment on the heave plate can effectively reduce the velocity and influence range of the fluid vortices induced by vertical motion near the heave plate. In the following sections, the influence of edge-cutting treatment is further clarified by analyzing the flow characteristics around the heave plate.

By comparing Figs. 20(c) and 23(a), it can be seen that the fluid blocking region at the leading edge of Configuration 2 does not show a significant optimization effect compared with that at the leading edge of the heave plate of Configuration 6; in fact, it can even be observed that the distribution area of the blocking region increases in the transition zone between the serrated structure and the edge-cutting treatment. In the latter half of the wave period, as the platform gradually returns to the vicinity of the equilibrium position, the fluid blocking region on the edge-cutting side at the leading edge of Configuration 2 dissipates at a relatively fast rate. Meanwhile, this process exerts an influence on the fluid blocking region at the serrated heave plate, driving its synchronous dissipation, thus effectively reducing the coverage range and maximum velocity of the fluid blocking region. Based on the structural characteristics, it can be inferred that such influence stems from the difference in the damping effect of the serrated heave plate and the edge-cutting treatment on the fluid. The results of the fluid velocity component in the y-axis direction are selected as the verification basis in this paper, see Fig. 24.

By comparing Figs. 20(a) and 23(b), it can be seen that edge-cutting improves the flow near the leading edge of the CFPSO over almost the entire wave period. In the leading edge region of Configuration 4, obvious fluid blocking areas are generated almost only in the lower left region and directly above the region. This is because the presence of the opening basically blocks the influence of the fluid on the lower right side on the fluid on the upper right side, while the low-damping characteristic of edge-cutting can inhibit the occurrence of fluid blocking. The combination of the two produces a more intense effect, so that the translational motion and rotation of the CFPSO in the x-axis direction will be effectively reduced. So far, the reasons and characteristics of edge-cutting structures in improving platform motion, as well as the internal reason for the superior damping effect of combined edge-cutting and opening structures, have been clearly elucidated.

4.6. Pitch characteristics

In CFD computations, the wave-induced loads acting on the CFPSO are mainly composed of two components, namely the pressure term and the viscous term, with the pressure term being significantly larger than the viscous term. The surface pressure acting on the CFPSO can be further decomposed into two parts: the dynamic pressure and the hydrostatic pressure. Since the time-history curves and RAO results presented earlier have basically indicated that the heave motion differences among the six types of CFPSOs are negligible, their vertical positions at each moment are approximately the same, and thus only the dynamic pressure component is discussed herein. The dynamic pressure results on the wave-facing surfaces of Configuration 1, Configuration 5, and Configuration 6 are illustrated in Fig. 25 below. In addition, the time-history results of pitching moment are obtained by integrating the dynamic pressure results of the CFPSO over its surface, as illustrated in Fig. 26 below.

By comparing Fig. 25, it can be seen that the opening structure exerts

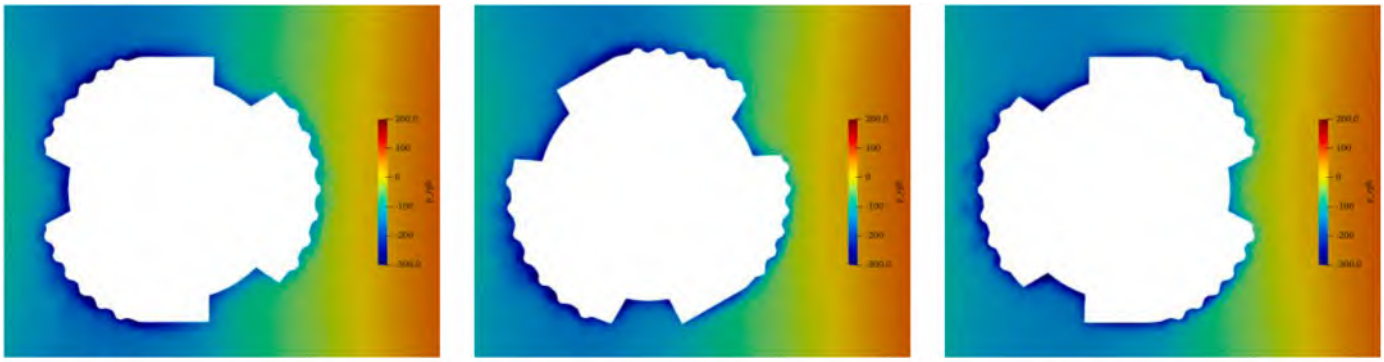

Fig. 21. Horizontal flow field around heave plate of Configuration 1, Configuration 5, Configuration 6.

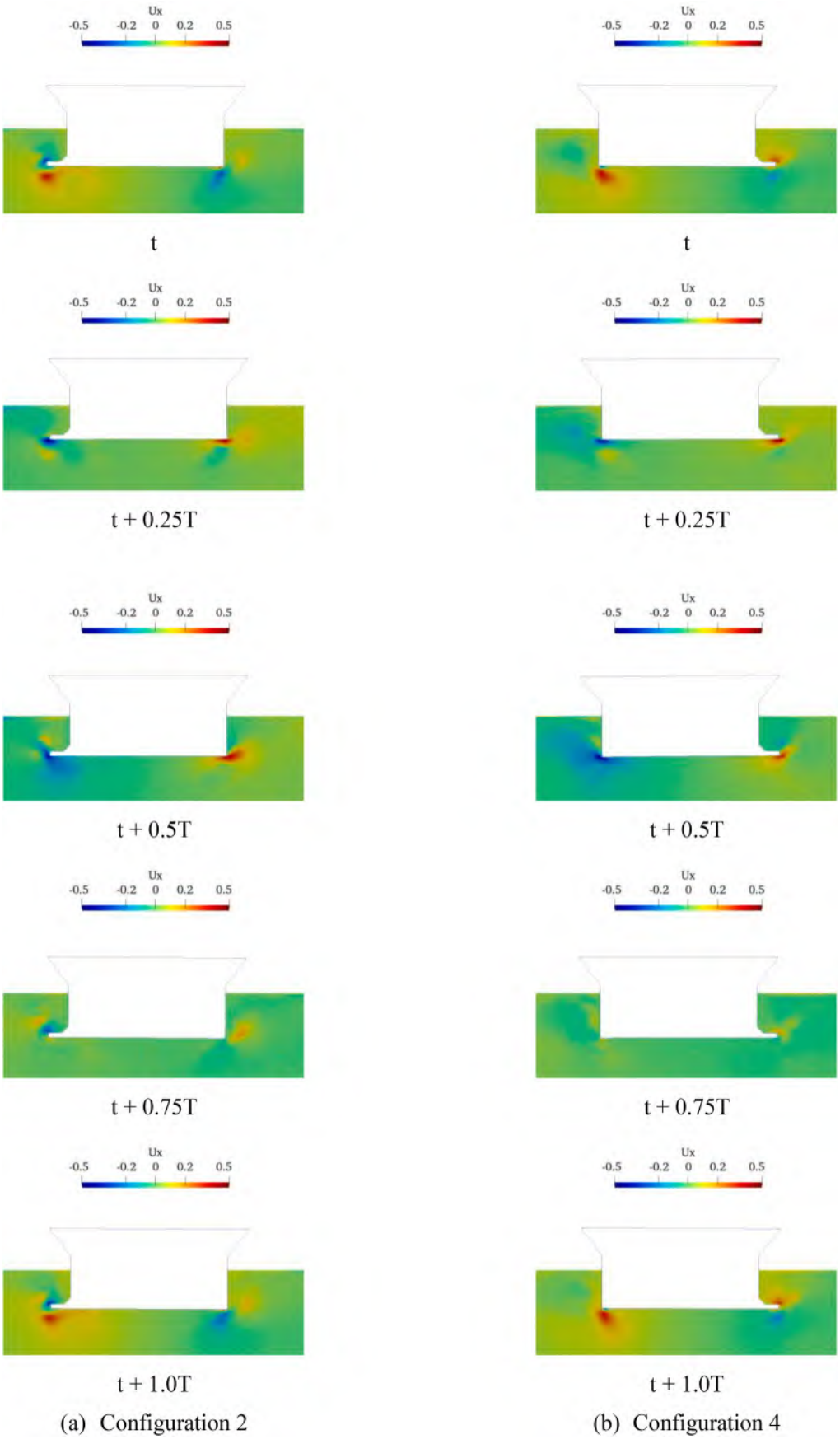

Fig. 22. Horizontal flow field around Configuration 2, Configuration 4 in XoZ plane.

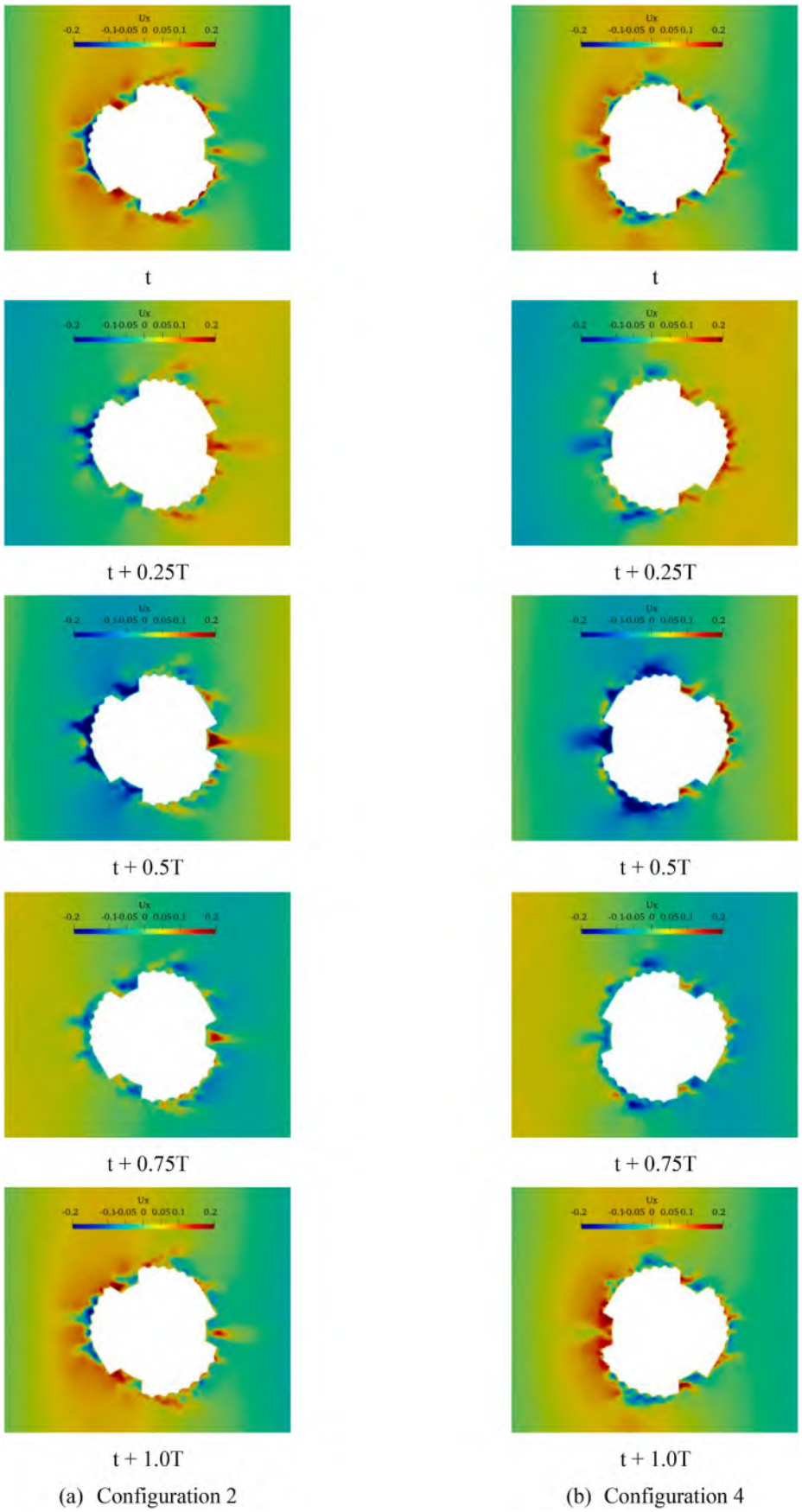

Fig. 23. Horizontal flow field around heave plate of Configuration 2, Configuration 4.

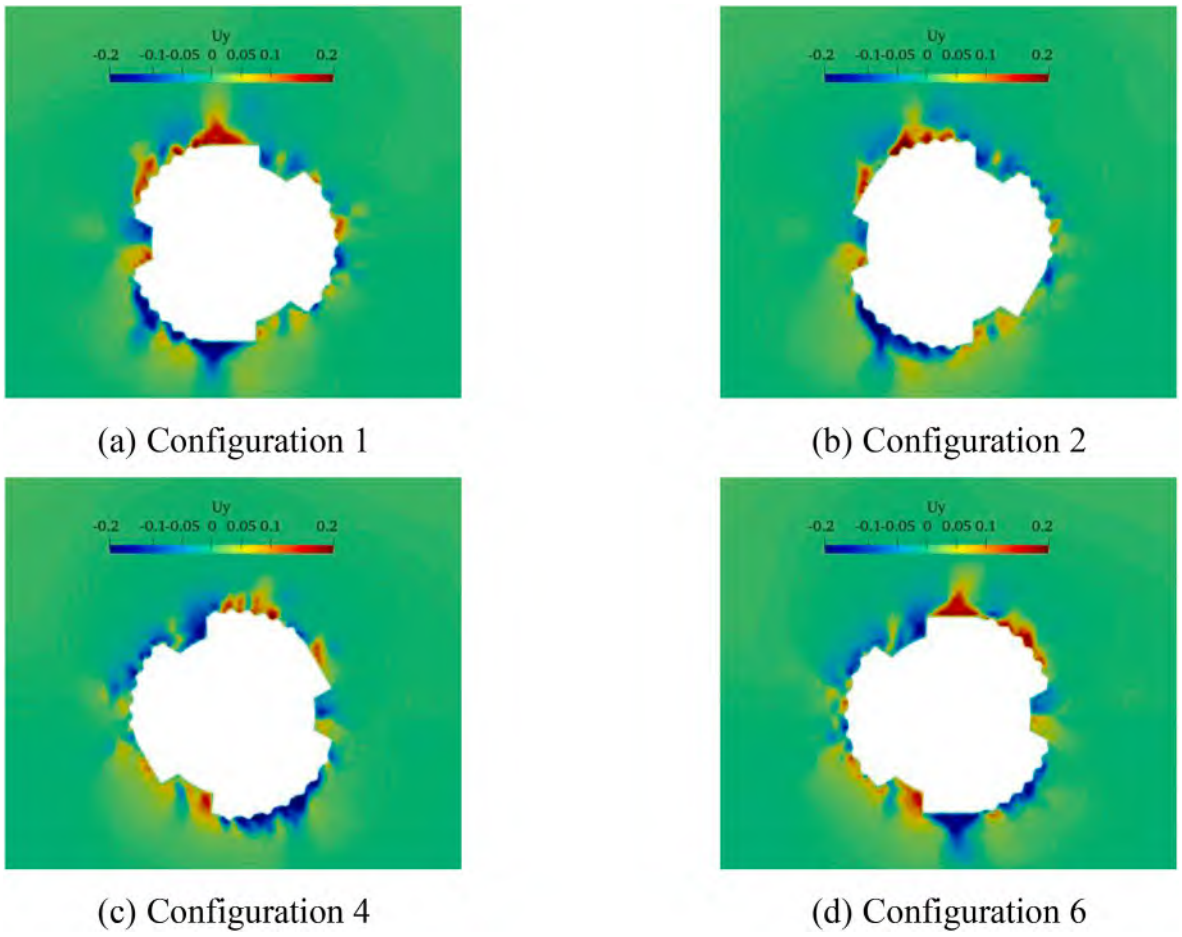

Fig. 24. Vertical flow field around the heave plate of CFPSOs.

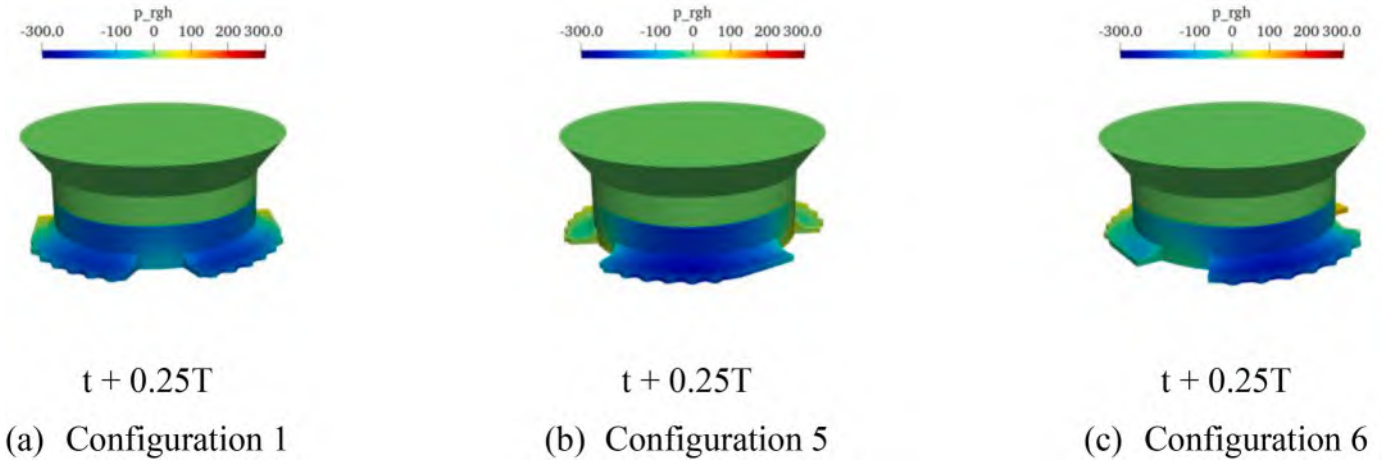

Fig. 25. Horizontal flow field around heave plate of Configuration 1, Configuration 5, Configuration 6.

an influence on the dynamic pressure distribution on the surface of the CFPSO, and the dynamic pressure in the area above the opening is significantly lower than that in the area above the serrated heave plate. This is because during the motion of the CFPSO, the extended part of the serrated heave plate acts on the water body above it, thereby forming a forward-moving high-velocity fluid vortex in front of the cylinder. When the opening is directly aligned with the wave incident direction, the low-pressure zone is distributed in the exact middle of the cylinder. As the opening deviates from the incident direction, the influence of the low-pressure zone gradually diminishes until it disappears. In fact, the distribution of the dynamic pressure low-pressure zone along the wave incident direction is rather detrimental to the pitching stability of the platform. Therefore, as the deviation degree of the opening from the wave-facing direction increases gradually, the pitching motion amplitude of the platform decreases accordingly. Ultimately, this conclusion is also verified by the statistical results of the time-history moments acting on the CFPSO.

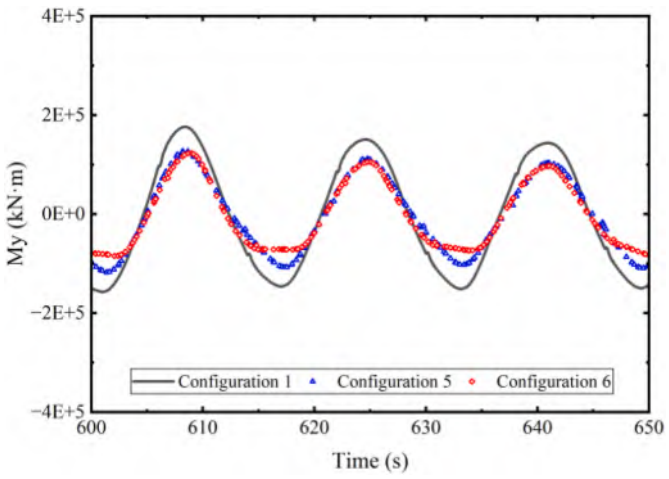

Fig. 26. Pitch moment results of CFPSO.

4.7. Wave period effects

Based on the analysis results of the time-history curves of the stable motion segment at the natural heave period T = 16 s and the specific flow field results presented earlier, the influence law of different structural characteristics of the wave-facing heave plate of the CFPSO on the platform motion response can be preliminarily elaborated. In this section, the response amplitude curves of the surge, heave, pitch and slow-drift motions of the CFPSO under other wave periods will be further presented, and an in-depth discussion will be conducted on whether the aforementioned conclusions are generally applicable to different wave periods. Among these results, the motion response amplitude results are shown in Fig. 27, and the slow-drift motion results are shown in Fig. 28.

Fig. 27(a) shows that under wave action, the surge motion response

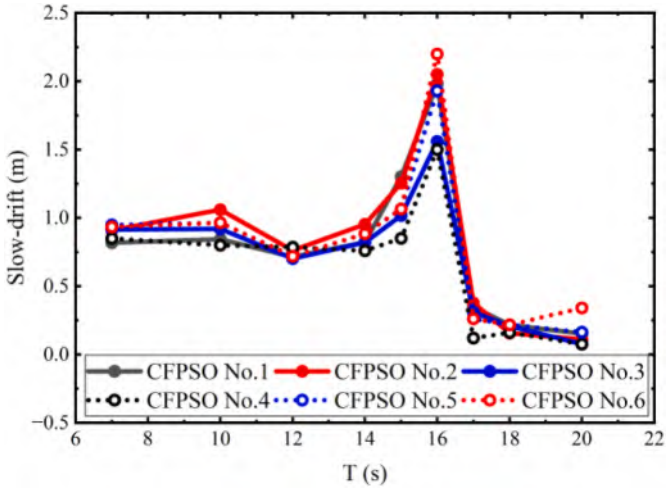

Fig. 28. Slow-drift response with different configurations under different wave periods.

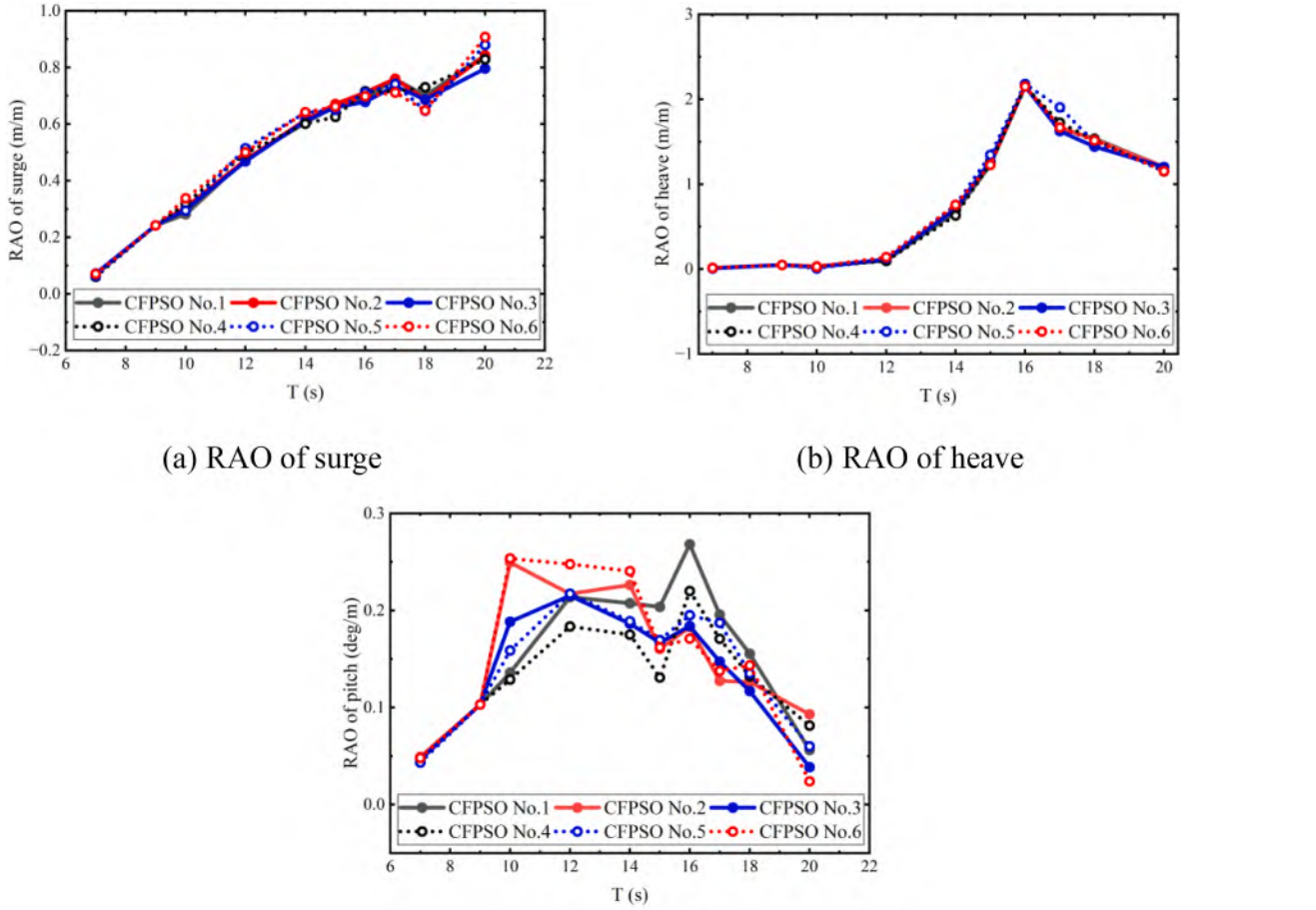

Fig. 27. Motion response amplitude result.

amplitude of the CFPSO gradually increases as the wave period increases. The influence of different wave-facing heave plate structural characteristics of the CFPSO on the surge motion amplitude is generally negligible within the wave period range of $T \in (7\ \text{s}, 17\ \text{s})$. There is a certain influence at wave periods of $T = 18$ s and $T = 20$ s, but it is not significant. Fig. 27(b) shows that different wave-facing heave plate structural characteristics of the CFPSO have basically no influence on the heave motion amplitude. Fig. 27(b) indicates that the pitch motion is significantly affected by both the wave period and the structural characteristics of the wave-facing heave plate. Fig. 27(c) indicates that the pitch motion is significantly affected by both the wave period and the structural characteristics of the wave-facing heave plate. First, two peaks appear in the pitch RAO curves of all six models, which occur within the wave period range of $T \in (10\ \text{s}, 14\ \text{s})$ and at period $T = 16$ s. The former exactly covers half of the natural pitch period, while the latter arises from the excitation of heave motion. Within the wave period range of $T \in (10\ \text{s}, 14\ \text{s})$, the pitch RAO of Configuration 2 and Configuration 6 are significantly higher than those of Configuration 3 and Configuration 5, while the pitch RAO of Configuration 1 and Configuration 4 are generally the smallest. That is, as the opening on the heave plate gradually deviates from the direction directly facing the wave incidence, the pitch RAO gradually decreases. When the wave period is $T \in (15\ \text{s}, 20\ \text{s})$, the result is basically consistent with the conclusion drawn from the previous time-history results: as the opening on the heave plate gradually deviates from the direction directly facing the wave incidence, the pitch RAO gradually increases. This indicates that different wave-facing heave plate structural characteristics may exert opposite influences within different wave period ranges. The specific reason by which the heave plate affects the pitching motion of the CFPSO will be further investigated and analyzed in future work, and the causes of the abnormal results observed within the small wave period range ($T \in (10\ \text{s}, 14\text{s})$) under specific incident angles will also be elucidated. However, by comparing the results of Configuration 1 and Configuration 4, Configuration 2 and Configuration 6, Configuration 3 and Configuration 5 pairwise, it can be seen that edge-cutting can still effectively improve the pitch RAO, and this inhibitory effect is still most significant when directly facing wave incidence.

Fig. 28 shows that the slow-drift curve presents a single-peak shape, and the peak arises from heave excitation. When the wave period is less than 16 s, the slow-drift is relatively large. As the wave period gradually increases, the slow-drift decreases significantly, and the horizontal motion is mainly manifested as surge. Under wave incidence with different periods, the conclusions drawn from the time-history results remain valid.

5. Conclusions

Relying on the in-house solver naoe-FOAM-SJTU, this paper numerically investigates the wave-induced motion responses and flow field characteristics of the CFPSO fitted with composite heave plates under regular waves. Taking model test results as the verification benchmark, systematic validations of mooring stiffness, grid convergence and time-step convergence are carried out.

Firstly, the CFPSO equipped with complex heave plates is compared with platforms fitted with six other types of heave plates. The comparison verifies that the CFPSO with complex heave plates outperforms the other platforms in motion performance. On this basis, the differences in motion responses caused by various wave-facing structural features of the CFPSO with complex heave plates are studied. The effects of edge-cutting, serrated protrusions and opening structures on platform motions are further analyzed. Combined with flow field data, the flow characteristics and coupling effects near the serrated protrusions, edge-cutting zones and openings are explored to clarify the action mechanism of each structural feature on platform motion responses. Meanwhile, the reliability of the conclusions drawn in this paper is verified by calculation results under other wave periods. The main conclusions of this paper are summarized as follows:

(a) The CFPSO with complex heave plates exhibits remarkable superiority in hydrodynamic motion performance compared with structures fitted with circular heave plates and other configurations. It can significantly suppress the first-order pitch motion, low-frequency surge and slow-drift motion without aggravating the heave response.

(b) The structural characteristics of heave plates on different wave-facing sides basically have no effect on the surge and heave RAO of the CFPSO, but mainly affect the pitch RAO. When the wave period is equal to the natural heave period, as the opening gradually deviates from the wave incidence direction, the pitch motion decreases gradually. Combined with the pressure distribution nephogram, this is because the extended outer edge of the serrated heave plate causes obvious forward high-velocity fluid eddies to appear in front of the cylinder, which reduces the overall wave-induced moment on the CFPSO, thereby making the pitch motion more stable.

(c) The influence of different structural characteristics of heave plates on the wave-facing side on the low-frequency motion of the CFPSO is mainly reflected in the slow-drift motion. When the entire serrated heave plate is directly facing the wave incidence direction, the slow-drift motion is the most significant, followed by the case where the opening is directly facing the wave incidence direction. When the combination of the opening and the edge-cutting heave plate is directly facing the wave incidence direction, the slow-drift motion is the smallest. An obvious fluid blocking zone is formed at the leading edge of the serrated heave plate, while almost no fluid blocking zone is generated when the opening is directly facing the wave incidence, resulting in a smaller horizontal wave force acting on the platform. The combination of the opening and the serrated heave plate destroys the symmetry of the fluid velocity distribution. Since the slow-drift force on the CFPSO along the x-axis direction is only the x-axis component of the actual horizontal wave force, the slow-drift motion is thus reduced.

(d) Independently arranging edge-cutting on the heave plate has an insignificant influence on the CFPSO. However, the edge-cutting structure on the wave-facing side of complex heave plates shows a noticeable effect. Especially when the opening structure on the wave-facing side directly faces incident waves within the wave incidence period range of 7–20 s, the motion suppression performance of edge-cutting is remarkably amplified. Compared with the serrated heave plate, edge-cutting itself generates a weaker fluid blocking effect, while the fluid blocking zone formed at the leading edge of the serrated heave plate disturbs the flow field distribution adjacent to the edge-cutting. When the opening faces incident waves directly, it is sandwiched between the edge-cutting structure and the serrated heave plate, isolating the disturbance imposed by the fluid blocking zone at the leading edge of the serrated plate on the flow field of the edge-cutting side and consequently greatly strengthening the vibration suppression capacity of edge-cutting.

CRediT authorship contribution statement

Yisheng Yao: Writing – original draft, Visualization, Validation, Methodology, Data curation. **Jingwen Zhang:** Visualization, Validation, Investigation, Formal analysis. **Gang Li:** Validation, Investigation, Formal analysis, Data curation. **Weiwen Zhao:** Writing – review & editing, Supervision, Software, Resources, Investigation, Funding acquisition, Conceptualization. **Decheng Wan:** Writing – review & editing, Supervision, Project administration.

Data availability

The data that support the findings of this study are available from the corresponding author upon reasonable request.

Author declarations

Authors have no conflict of interest to declare.

Declaration of competing interest

The authors declare that they have no known competing financial interests or personal relationships that could have appeared to influence the work reported in this paper.

Acknowledgements

This work is supported by the National Key Research and Development Program of China (Grant No 2025YFF0519800), and National Natural Science Foundation of China (No 52131102), to which the authors are most grateful.

References

Deng, S., Cai, Y., Yang, X., Song, Z., Yang, G., 2022a. Experimental study on the effects of wave and current interaction on vertical motions of a cylindrical FPSO. In: The 32nd International Ocean and Polar Engineering Conference (OnePetro).

Deng, S., Zhong, W., Yang, X., Wu, M., Fu, S., 2022b. Experimental and numerical study of the hydrodynamic features of a cylindrical FPSO considering current-induced motion. Ocean. Eng. 262, 112263.

Devolder, B., Rauwoens, P., Troch, P., 2017. Application of a buoyancy-modified k-ω SST turbulence model to simulate wave run-up around a monopile subjected to regular waves using OpenFOAM. Coast. Eng. 125, 81–94.

Fontaine, E., Orsero, P., Ledoux, A., Nerzic, R., Prevosto, M., Quiniou, V., 2013. Reliability analysis and Response Based Design of a moored FPSO in West Africa. Struct. Saf. 41, 82–96.

Gonçalves, R., Fujarra, A., Rosetti, G., Nishimoto, K., Cueva, M., Siqueira, E., 2009a. Vortex-Induced motion of a Mono-Column platform: new analysis and comparative study. In: Proceedings of OMAE2009, 28th International Conference on Ocean. Offshore and Arctic Engineering, Honolulu, Hawaii.

Gonçalves, R., Matsumoto, F., Malta, E., Rosetti, G., André, L., Fujarra, C., Nishimoto, K., 2009b. Evolution of the MPSO (Mono-Column production, storage and offloading system). Mar. Syst. & Ocean Technol. 5, 45–53.

Gu, J., Xie, Y., Zhao, Y., Li, W., Tao, Wen, Huang, X., 2018. Study on vortex-induced motions of A new type of deep draft multi-columns FDPSO. China Ocean Eng. 32, 1–13.

Guilmineau, E., Queutey, P., 2002. A numerical simulation of vortex shedding from an oscillating circular cylinder. J. Fluid Struct. 16 (6), 773–794.

Han, Seung-Yoon, Bouscasse, Benjamin, Vincent, Leroy, Delacroix, Sylvain, Gilloteaux, Jean-Christophe, Bonnefoy, Félicien, Le Touzé, David, 2024. Experimental study of hydrodynamic loads induced by the motion of a vertical circular cylinder with heave plates in proximity of the free surface. Ocean Eng. 310 (Part 2), 118712.

Huo, S., Deng, S., Song, Z., Zhao, W., Wan, D., 2023. On the hydrodynamic response and slamming impact of a cylindrical FPSO in combined wave-current flows. Ocean Eng. 275, 114139.

Ji, X., Yan, L., Tang, Y., Tong, B., 2019. Viscous damping effectand vortex shedding performance of the novel anti-motion structures on a cylindrical FPSO. Ocean. Eng. 190, 106430.

Ji, Yiming, Tong, Linlong, Zhang, Jisheng, Li, Haoran, Chen, Hao, Guo, Yakun, Xie, Shoupeng, 2026. Experimental study of the seabed responses induced by a floating column with a heave plate. Coast. Eng. 206, 104967.

Li, B., Huang, Z., Low, Y., Ou, J., 2013b. Experimental and numerical study of the effects of heave plate on the motion of a new deep draft multi-spar platform. J. Mar. Sci. Technol. 18, 229–246.

Li, J., Liu, S., Zhao, M., Teng, B., 2013a. Experimental investigation of the hydrodynamic characteristics of heave plates using forced oscillation. Ocean. Eng. 66, 82–91.

Liu, Y., Miao, G., 1985. Second-order wave force on a two-dimensional object. Ship Building of China.

Maccamy, R., Fuchs, R., 1954. Wave Forces on Piles: a Diffraction Theory. Beach Erosion Board.

Medina-Manuel, Antonio, Kristiansen, Trygve, Maron-Loureiro, Adolfo, Molina Sánchez, Rafael, Souto-Iglesias, Antonio, 2025. A comparative experimental study of the hydrodynamic force on a solid heave plate, and on heave plates with regularly distributed and fractally distributed perforations. Appl. Ocean Res. 164, 104787.

Saad, A., Joao, L., Loureiro, R., Brandao, R., Filho, R., Lopes, C., Gioppo, H., 2009. Motion behaviour of the Mono-Column FPSO sevan piranema in Brazilian waters. Paper Present Offshore Technology Conference. Houston, Texas.

Sathia, R., Vijayalakshmi, R., 2019. Effect of keel plate on the performance of FPSO suitable for Arctic Ice environment. Ships Offshore Struct. 963–973.

Subbulakshmia, A., Jose, J., Sundaravadivelu, R., Selvam, R., 2015. Effect of viscous damping on hydrodynamic response of spar with heave plate. Aquat. Procedia 4, 508–515.

Tao, L., Cai, S., 2004. Heave motion suppression of a Spar with a heave plate. Ocean. Eng. 5–6 (31), 669–692.

Tao, L., Molin, B., Scolan, Y., Thiagarajan, K., 2007. Spacing effects on hydrodynamics of heave plates on offshore structures. J. Fluid Struct. 23 (8), 1119–1136.

Wang, J., Wan, D., 2018. CFD investigations of ship maneuvering in waves using naoe-FOAM-SJTU Solver. J. Mar. Sci. Appl. 17 (3), 443–458.

Wang, J., Zhao, W., Wan, D., 2019. Development of naoe-FOAM-SJTU solver based on OpenFOAM for marine hydrodynamics. J. Hydrodyn. 31 (1), 1–20.

Wang, L., Wang, W., Du, Y., Gao, H., Yi, H., 2017a. Motion problem induced by dynamic positioning system for new sandglass-type floating body. J. Mar. Sci. Technol. 22, 162–175.

Wang, W., Du, Y., Wang, L., Huang, Y., 2017b. Wave-free characteristic of heave motion response for new sandglass-type model. Ships Offshore Struct. 13 (2), 181–193.

Wang, W., Wang, L., Du, Y., Yao, Y., Huang, Y., 2016. Numerical and experimental analysis on motion performance of new sandglass-type floating body in waves. Mar. Struct. 46, 56–77.

Wei, Y., Yang, J., Chen, G., Hu, Z., 2011. The effect of axial stiffness of mooring lines on the horizontal motion of FDPSO. Sci. China Phys. Mech. Astron. 54 (1), 10–15.

Wei, Y., Yang, J., Chen, G., Hu, Z., 2012. Experimental study on the hydrodynamic performance of FDPSO and SRV. Ships Offshore Struct. 7 (4), 357–369.

Yang, C., Lu, Z., Wan, C., Su, Z., Bai, X., Johanning, L., 2025. Semi-analytical study on the hydrodynamic performance of a cylindrical moon column FPSO with damping plate. Ocean. Eng. 316, 119894.

Yue, M., Liu, Q., Li, C., Ding, Q., Cheng, S., Zhu, H., 2020. Effects of heave plate on dynamic response of floating wind turbine Spar platform under the coupling effect of wind and wave. Ocean Eng. 201, 107103.

Zhang, S., Ishihara, T., 2018. Numerical study of hydrodynamic coefficients of multiple heave plates by large eddy simulations with volume of fluid method. Ocean Eng. 163, 583–598.

Zhang, Wenzhe, Calderon-Sanchez, Javier, Almeida-Medina, Tanausú, Medina-Manuel, Antonio, Souto-Iglesias, Antonio, 2025. Numerical analysis of forced heave oscillations for an FOWT column with a heave plate using overset mesh. Ocean Eng. 341 (Part 4), 122736.

Zhao, W., Wang, J., Wan, D., 2020. Vortex identification methods in marine hydrodynamics. J. Hydrodyn. 32 (2), 286–295.